AD-A170 157

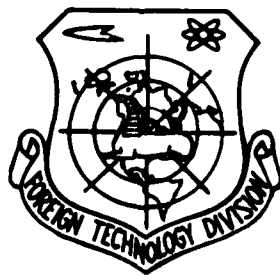# FOREIGN TECHNOLOGY DIVISION

ACTA AERONAUTICA ET ASTRONAUTICA SINICA

(Selected Articles)

DTIC

JUL 3 0 1986

E

DTIC FILE COPY

86 7 28 130

HUMAN TRANSLATION

Ac......... for

Dist

A-l

QUALITY
INSPECTED
4

Table of Contents

> Partial contents:

GRAPHICS DISCLAIMER

All figures, graphics, tables, equations, etc. merged into this
translation were extracted from the best quality copy available.

Wind Tunnel Experimental Investigation on Spanwise Blowing

Harbin Aerodynamics Research Institute

Tian Xueshi, Li Xiangrui and Zhao Jincheng

Abstract

In this work the aerodynamic effects of the spanwise blowing of a whole delta wing aircraft and the flap spanwise blowing of a wing model in an FL-8 and an FL-5 wind tunnel were analyzed. In addition, they were compared to the blown flap results obtained with the same models in the same wind tunnels.

It was found that the vortex generated is a shoulder vortex, instead of a jet vortex, when spanwise blowing is applied to a flap with a large angle of deflection. It was pointed out that vortex control is the important reason for the lift increment due to spanwise blowing and it is not merely a boundary layer control problem. By means of optimizing nozzle shape and parameters, it is possible to use current engines to provide a small jet momentum coefficient (approximately 0.012) to obtain a similar lift increment as that of a blown flap. Thus, the landing performance of the aircraft may be improved. A "two branch nozzle" was used for the first time to improve the flow on the flap surface. Due to the fact that this technique has the advantages such as simple structure, light weight, no need to occupy internal space and high survivability, it is possible to become one of the more promising means to be selected to increase lift.

Major Symbols

S   wing area

δ_j trailing edge flap deflection angle

c_f trailing edge flap chord

q   incoming flow velocity pressure

P_0 total jet pressure at nozzle

$P.$ static pressure of flow in experimental section of wind tunnel

ε downwash angle

α attack angle

G_B and m   weight and mass flow of jet, respectively

d_n, h_n, x_n, θ_n, Λ_n, F_n nozzle inner diameter, distance between nozzle center to wing surface, nozzle surface, nozzle chord direction (using flap rotating axis as origin), angle between nozzle center line and flap surface, sweepback angle of nozzle center line and effective nozzle area, respectively.

V_j nozzle flow velocity (assuming isentropic expansion)

/358

$$V_j = \sqrt{\frac{2gk}{k-1} RT_{\bullet} \left[1 - \left(\frac{P_{\bullet}}{P_{\bullet}} \right)^{\frac{k-1}{k}} \right]} \tag{A}$$

$C_\mu = \dot{m}V_j/qS$ jet momentum coefficient

Δ aerodynamic force increment due to blowing

Introduction

Spanwise blowing (SWB) is a new technique to control separation vortex. Spanwise blowing across the wing can control the leading edge separation vortex. Spanwise blowing across the flap and the rudder is considered to belong to the domain of boundary layer control in references [2,3]. In other countries, the focal point of research is placed on SWB of the wing with the hope that the maneuverability at large angles can be improved instead of using strake. Flap and rudder SWB may result in significant gains under low flow conditions[1]. Flap SWB (SWBF) may be developed to replace the complicated blown flap system. In 1982 to 1983, we used a large delta wing aircraft model to complete SWBF force and flow pattern experiments. The purpose was to reveal the flow mechanism of SWBF and to investigate its lift increasing potential. In addition, the results were compared to those obtained in blown flap experiments (from this point on it is called experiment [A]) completed in 1980 by using the same model in the same wind tunnel in order to evaluate the current practical values of SWBF.

II.   Experimental Apparatus and Model

The FL-5 low speed wind tunnel is an open re-circulating tunnel. The cross-section of the experimental section is circular and is 1.5m in diameter. The FL-8 wind tunnel is a closed re-circulating type. The cross-section of its experimental section is a flat octagon 3.5 x 2.5 m in size. The

wing model used is a sharp delta wing. The aspect ratio is 2.22 and the span is 1.79m. The flap is rectangular and its aspect ratio is 1.65. The principal support point of the model was located at 36.3% of the mean aerodynamic chord b_A. This model has blown flap and SWB capabilities. It is capable to perform spanwise blowing on the flap, wing, auxiliary wing, horizontal tail, and rudder, as shown in Figure 1.
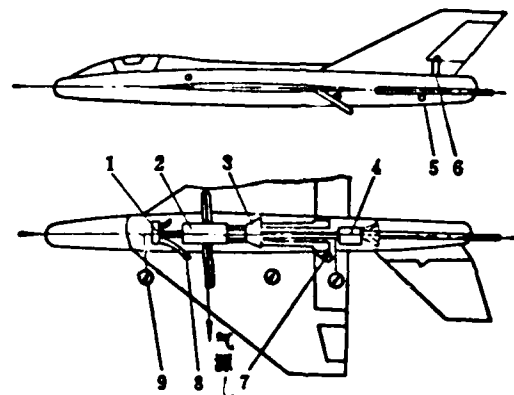
Figure 1. Planview of Nozzles and Air Supply System of Spanwise Blowing Model

    1. Plenum for wing spanwise blowing
    2. Air passage joint
    3. Plenum for flap spanwise blowing
    4. Tail plenum
    5. Nozzle for horizontal tail blowing
    6. Nozzle for rudder blowing
    7. Nozzle for flap blowing
    8. Nozzle for wing blowing
    9. Pressure gauges
  10. Air supply

There are four types of SWBF nozzles: (1) single nozzle: diameter and sweepback angle can be changed; (2) three branch nozzle with the same root: any branch can be blocked by wood; (3) multi-hole nozzle: it is made by sealing a 120 mm long copper pipe and installed on the inside edge of the flap. An array of holes were drilled in parallel to the upper flap surface; and (4) moving nozzle: it is made by bending a 5.5mm inner diameter copper pipe. 1-2 of this type of nozzles are moved over a large range across the flap to observe the flow pattern. During blowing, δ_f is 45° or 60°. The installation of the half-wing model in the FL-5 wind tunnel and that of the whole aircraft model in the FL-8 wind tunnel are shown in Figures 2 and 3, respectively. The air supplies are air pump and air compressor, respectively.

Figure 2. Mounting of Half-wing Model with Spanwise BLowing in FL-5 Wind Tunnel

Figure 3. Mounting of Whole Aircraft Model With Spanwise Blowing in FL-8 Wind Tunnel

III. Experimental Method and Data Processing

In the FL-5 wind tunnel, techniques such as helium bubbles, space screen, fuel flow, water mist, long filament ball, etc., were used to conduct flow condition experiments. The wind speed was 5~35 m/sec, the angle of attach was 10°. Force measurement and fluorescent microfilament flow condition experiments were accomplished in the FL-8 wind tunnel. The maximum wind velocity was 40 m/s, Re=2.74x10^{6}. Angle of attach range was $-2\sim18^{\circ}$. Preparations included calibration of nozzle pressure, measurement of effect area of nozzle and measurement of support interference. The ground effect experiment simulated the state of the instance the landing gear leaves the ground. In the experiment, $C_{\mu_\bullet}$ was controlled through controlling the pressure.

$$C_\mu = \begin{cases} \left| \dfrac{F_\bullet}{qs} P_0 \left(\dfrac{P_\bullet}{P_0} \right)^{\frac{1}{k}} \dfrac{2k}{k-1} \left[1 - \left(\dfrac{P_\bullet}{P_0} \right)^{\frac{k-1}{k}} \right] \right. & \text{(subcritical state, } P_0/P_a < 1.893) \\[3mm] \left| \dfrac{F_\bullet}{q \cdot s} P_\bullet k \sqrt{\left(\dfrac{2}{k-1} \right)\left(\dfrac{2}{k+1} \right)^{\frac{k+1}{k-1}} \left[1 - \left(\dfrac{P_\bullet}{P_\bullet} \right)^{\frac{k-1}{k}} \right]} \right. & \text{(supercritical state, } P_0/P_a \geq 1.893) \end{cases}$$

6

IV. Flow Pattern Analysis and Concept of "Shoulder Vortex"

Using the surface or spatial flow pattern display techniques mentioned above, it is possible to observe the effect of flap blowing on the flow separation and downwash flow field. When δ_j = 45° or 60°, the flap is totally separated prior to blowing. The streamlines are flat over the flap. When $a = 10°$, the primary wing already has a leading edge vortex of considerable strength. After blowing, the washdown on the flap increased after blowing. The streamlines are nearly parallel to the flap surface.

It is believed that there is a weak "jet vortex" on the flap according to reference [2] ($a=12°$, $\delta_j = 40°$) which transforms the flap spanwise blowing jet to a spinning jet vortex. Furthermore, it is pointed out that the jet vortex rapidly rolls up to form a strong vortex after it leaves the outer edge of the flap. The vorticity of the jet vortex comes from the separation caused by the "bar er effect" of the jet. The "carryover effect" of the jet provides axial velocity to small diverging vortices. Thus, a concentrated vortex appears (immediately) following the jet, i.e., a jet vortex. In this work, we proved with oil flow pattern experiment that the jet vortex does not exist behind the jet from a single nozzle applied to a flap with large deflection angles ($a = 10°$, $\delta_j = 45°$). In front of the jet (not necessarily adjacent to it), there is a concentrated vortex of considerable /360 strength. In this work, it is named as the "shoulder separation vortex" (or "shoulder vortex"). The cause of its formation is that vorticity is supplied from the flap shoulder separation

7

(primary separation) of the flow. The carry over effect of the jet, however, provides axial velocity to the vortex. Thus, the condition for the creation of a stable three-dimensional vortex is in place to form a concentrated shoulder vortex. Figure 4 shows the oil flow pattern caused by single nozzle blowing. The V-shaped oil pattern in front of the jet is the trace swept by the shoulder vortex. Long silk balls (several cotton balls are hung on silk threads) placed in the jet region did not rotate. When they were placed in the V-shaped oil pattern region, they began to spin rapidly. When helium bubbles entered the vortex area, we could also see the bright line of rotation. Similarly, the shoulder vortex could also be seen on the spatial silk screen.

Figure 4. Oil Flow Pattern Caused by Single Nozzle Blowing
$(C_\mu = 0.012)$

The shoulder vortex is located in front of the jet. They are frequently separated by a certain distance on the inside of the flap. This distance may even be very large. On the outside of the flap, they get very close and may merge into one. A jet vortex, however, is always behind the jet. In addition, it is always adjacent to the jet. From the oil flow pattern caused by moving nozzle located at $63\% c_f$ (see Figure 5), we can see that the shoulder vortex extends from the root of the flap shoulder. It is far away from the jet. They begin to merge on the outside of the flap. When $\delta_j = 24^o$, there is no flap flow separation without spanwise blowing. In this case, spanwise blowing will not generate a shoulder vortex. Instead, a jet vortex appears following the jet. All the above mentioned experiments proved that a shoulder vortex is not a jet vortex. In reference [4], although the concept of shoulder vortex was not identified, yet it was observed that the concentrated vortex was located in front of the jet.
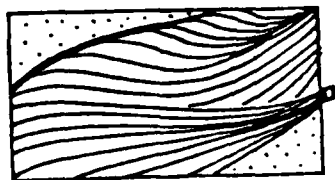

Figure 5. Oil Flow Pattern Caused by Aft-position Nozzle Blowing
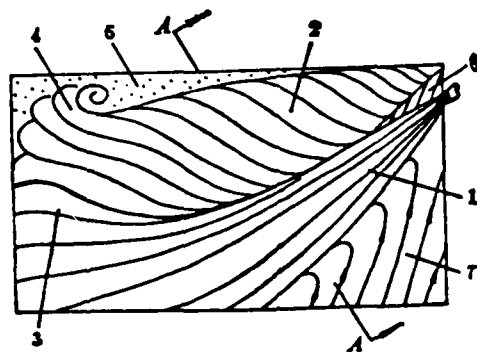
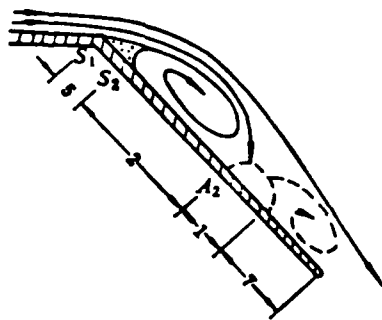Figure 6. Flow Pattern on Upper Surface of the Flap with Single
Nozzle Blowing

Figure 7. Sectional Flow Pattern of the Flap with Single Nozzle
Blowing

10

Figures 6 and 7 are the plane flow pattern and sectional flow pattern caused by single nozzle blowing corresponding to Figure 4. Region "1" is the jet region, "2" is the shoulder vortex region, "3" is the shoulder vortex merged into the jet, "4" is the separation spiral point, "5" is the dead region /361 between the primary separation line S_1 (shoulder line) and secondary separation line S_2, "6" is the re-adhesion region and "7" is the re-circulation region. The oil flow patterns obtained in C_μ range from 0.006~0.024 are similar to Figure 4. In order to eliminate the re-circulation region, a two branch nozzle was used. The pattern corresponding to the oil flow photograph is shown in Figures 8 and 9. $C_\mu = 0.012$. Regions "1" and "2" are the first and second jet region, respectively. Region "3" is the shoulder vortex. Region "4" is the second concentration vortex. Regions "5" and "6" are the shoulder vortex and second concentration vortex already merged with the jets, respectively. Region "7" is the flap root vortex. "8" is the boundary node. Region "9" is the boundary flow region. "10" is the separation spiral point. Region "11" is the dead region. The second concentrated vortex is a special phenomenon created by the installation of the second jet. For a three branch nozzle, there are three vortices on the oil flow pattern picture: shoulder vortex, second and third concentration vortices.
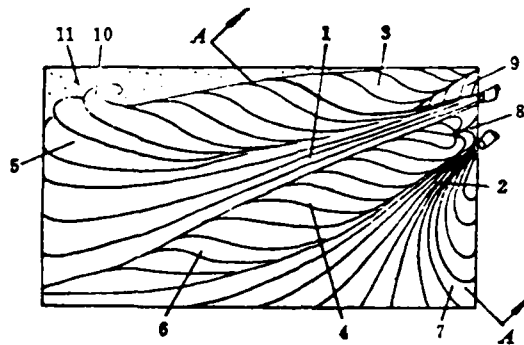
11

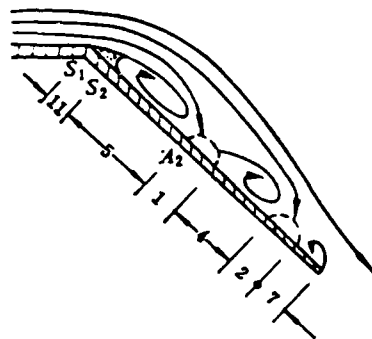Figure 8. Flow Pattern on Upper Surface of the Flap Blowing with a "Two Branch Nozzle"

Figure 9. Sectional Flow Pattern of the Flap Blowing with a "Two Branch Nozzle"

It was considered in references [2,3] that SWBF belongs to the domain of boundary layer control. The carry over effect of the jet brings the main stream to the vicinity of the jet to flow downstream along the surface of the flap to eliminate boundary layer separation. In reference [2], it was believed that the jet vortex is not very strong in the flap region. The contribution of the concentrated vortex to lift increment was not pointed out. In this work, we believe that SWBF is not the same as the flap flow pattern with chordwise blowing. In the former case, a very large portion of the upper flap surface is controlled by the vortex. In the latter case, with the exception of the wing tip vortex and root regions, the streamline is smooth over a large area. The basic flow pattern of SWBF at a large deflection angle is similar to that of SWB at a large attack angle. There is a dead region at the shoulder or the leading edge. It is followed by a large shoulder vortex or leading edge vortex and then by the jet region. We believe that the lift increase mechanism associated with SWBF is similar to that of SWB of the wing. The effect of vortex control exists in both cases. The difference is that in the former case the shoulder vortex directly controls the flap flow which indirectly controls the wing flow and in the latter case the leading edge vortex directly controls the wing flow. The life increment associated with SWBF is only partially supplied by SWBF. The other part is acting on the wing. The mechanism for the first part is similar to that of SWB. However, we do not deny that the direct carry over effect of the jet contributes toward the lift increment. The latter is caused by

13

the downward movement of the stationary point of the wing as a result of improvement of the flow surrounding the wing from flap blowing. In summary, the life increase mechanism of SWBF is not merely a simple boundary layer control problem.

V. Aerodynamic Characteristics of Spanwise Blowing of the Flap

(1) Lift-drag Characteristics. When $\alpha = 10^{\circ}$ and $C_{\mu} \leq 0.015$, $\Delta C_y = 0.1 \sim 0.14$ for the whole aircraft model, an increase of lift by approximately 20% as compared to that without blowing. Blowing has little effect on the slope of the lift line. Blowing will increase the drag. The lift to drag ratio decreases. The model we used in this work is similar to that used in the blown flap experiment [A]. In addition, in 1980 a 1.59m span model of similar profile was used in another blown flap experiment (experiment [B]) in the FL-8 wind tunnel. The lift increment produced by SWBF is similar to those of [A] and [B], as shown in Figures 10 and 11 and in Table 1. From the viewpoint of lift increase efficiency $\Delta C_y/C_{\mu}$, SWBF is not as high as blown flap. The order of magnitude of the latter has already reached the /362 maximum ΔC_{y_0} at $C_{\mu} = 0.003$. The effect on drag is comparable in either case. Most of the present fighters still use a single seam retracting flap. When the flap of this model was changed from a 24° single seam retracting flap to a 45° SWBF, lift could be increased by more than 20%. The lift increase ratio $\Delta C_y/C_y$, or lift increase efficiency $\Delta C_y/C_{\mu}$, has already approached or exceeded the results reported in references [2,3] by optimizing

14

the nozzle used.
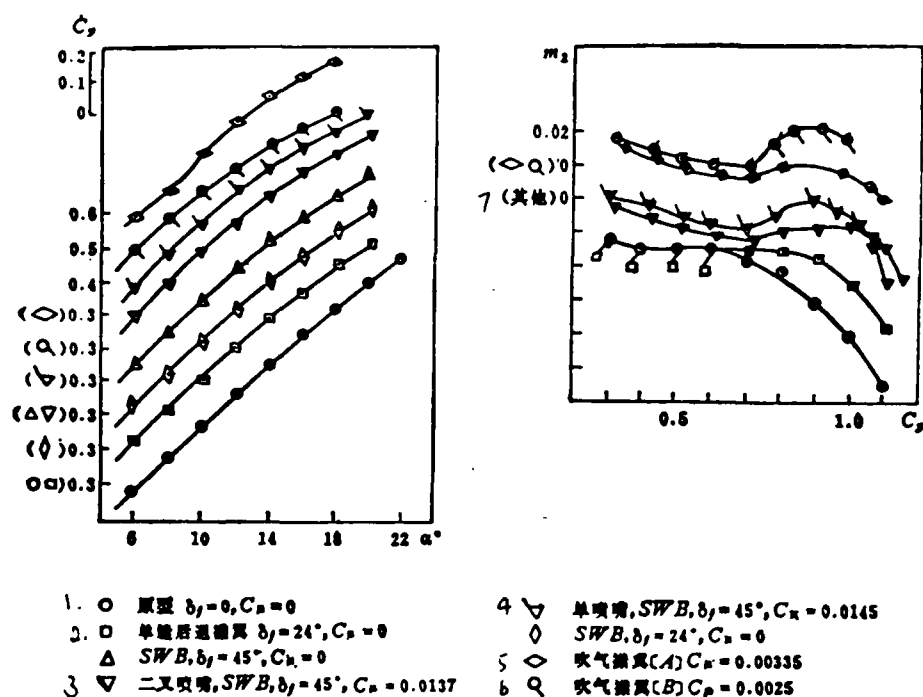
Figure 10. Comparison of Longitudinal Aerodynamic Character-
istics of Spanwise Blowing of the Flap and Blown Flap

1. o original model $\delta_f = 0$, $C_\mu = 0$

2. □ simple seam retracting flap $\delta_f = 24^O$, $C_\mu = 0$

3. ▽ two branch nozzle, SWB, $\delta_f = 45^O$, $C_\mu = 0.0137$

4. ⊽ single nozzle, SWB, $\delta_f = 45^O$, $C_\mu = 0.0145$

5. ◇ blown flap [A] $C_\mu = 0.00335$

6. Q blown flap [B] $C_\mu = 0.025$

7. Blown flaps

15

Table 1. Comparison of ΔC_y and ΔC_x of Spanwise Blowing of the Flap and Blown Flap ($\alpha = 10°$)

项 目 1.	SWBF 二叉喷嘴 2. $C_\mu = 0.0137$	吹气襟翼 [A] 3 $C_\mu = 0.00335$	吹气襟翼 [B] 4 $C_\mu = 0.0025$
$C_y(\alpha = 10°)$	0.79	0.79	0.77
$\Delta C_y(\alpha = 10°)$	0.14	0.14	0.12
$\Delta C_x(\alpha = 10°)$	0.07	0.082	0.062

1. item
2. SWBF two branch nozzle
3. blown flap [A]
4. blown flap [B]

(2) Pitching Moment Characteristics. Blowing makes the flap lift increase which produces a diving moment for a tailless aircraft. In addition, the focal point is shifted back by 2-4% b_A (mean aerodynamic chord). ε and ε^a in the horizontal tail region will increase. SWBF is similar to a blown flap. When the flap reflection angle increases from 24° to 45° with blowing, the stability decreases. The degree of stability of SWBF at angles of attack for take off and landing is between those in experiment [A] and experiment [B]. The stability is unsatisfactory as shown in Figure 10 and Table 2. When $\alpha = 10°\sim12°$, the downwash of SWBF is larger than that of a blown flap. The ε^a of the former is 0.13 larger than that of the latter. It is fortunate that the focal point of the wing-fuselage combination shifted backward by 4% b_A after SWBF is applied. In the case of a blown flap, it moves forward by approximately 2~5% b_A. In the linear region of the $m_z\sim C_y$ curve, the stabilities of all three parameters are very

16

close, approximately around -0.05. The diving moment of a single

seam retracting flap (24°) aircraft is approximately 0.01 larger

than that of 45° SWBF. The downwash of the former is smaller

than that of SWBF. The horizontal tail efficiencies, m_z^φ, are very

close in both cases. After applying SWBF and making it

horizontal, lift could still be increased by nearly 20%.
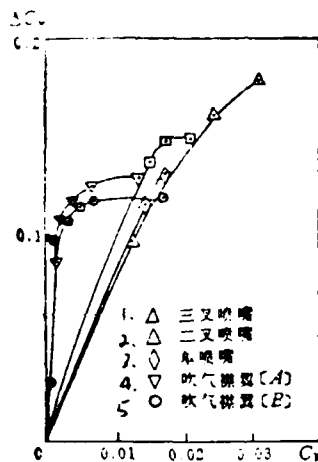

Figure 11.   Relation between ΔC_y and C_μ for Various Nozzles

    ($a=10^\circ$)

    1.   three branch nozzle
    2.   two branch nozzle
    3.   single branch nozzle
    4.   blown flap [A]
    5.   blown flap [B]

Table 2. Comparison of Pitching Moment Characteristics of Flap Spanwise Blowing and Blown Flap

項 目	SWBF二叉喷嘴	吹气襟翼[A]	吹气襟翼[B]	单缝后退襟翼24°
$m_x(\alpha = 10°)$	-0.019	-0.002	0.011	-0.03
$m_z^{cy}(\alpha = 10°)$	0.064	0.052	0.178	-0.03

1. item
2. SWBF two branch nozzle
3. blown flap [A]
4. blown flap [B]
5. single seam retracting flap 24°

(3) Transversal Effect. Blowing has little effect on the transversal characteristics. After $|\beta| > 10°$, m_x^β and m_y^β increase slightly. Besides, when an aircraft is symmetric, there is no non-symmetric transverse force and moment. The transversal stability of the aircraft is improved after SWBF is applied as compared to that of the single seam retracting flap.

(4) Ground Effect. The in tance at which the wheels of an aircraft leave the ground was simulated. Its aerodynamic characteristics and a comparison of situations with and without a ground board are shown in Table 3.

Table 3. Comparison of Aerodynamic Characteristics of Spanwise Blowing of the Flap With and Without Ground-board ($a=10^{\circ}$ except for C_y^d)

$\delta_f = 45^{\circ}$ 三叉喷嘴	C_a	C_y^c 线性段	C_y	ΔC_y	C_s	ΔC_s	k	m_z	Δm_z	$m_z^{C_y}$	$\Delta m_z^{C_y}$	$m_z^{\bullet}$
无地板	0	0.043	0.64		0.164		3.9	0.005		0.16		−0.0105
	0.0145	0.043	0.74	0.1	0.212	0.048	3.49	0.018	0.013	0.126	−0.034	−0.0115
有地板	0	0.055	0.82		0.158		5.19	−0.129		−0.065		−0.0084
	0.0145	0.057	0.92	0.1	0.234	0.076	3.93	−0.133	−0.004	−0.126	−0.061	−0.008

1. three branch nozzle
2. without ground board
3. with ground board
4. linear segment

VI. Conclusions

(1) When SWBF is used at large flap deflection angles ($\geq$ 40°~45°), a relatively strong vortex is formed in front of the jet. Its vorticity comes from shoulder separation and its axial velocity is a result of the carry over effect from the jet. It is called the shoulder vortex. This vortex has an important effect on the boundary layer and the external flow field. It has a control effect on the flap. Blowing on a layer deflective angle flap will not create a "jet vortex". The mechanism associated with the lift increase due to SWBF should not be concluded as the boundary layer control related to the carry over effect of the jet.

19

(2) The lift increment obtained due to SWBF comes from the flap as well as from the wing. The lift increment from the wing is primarily caused by improvement of the flow around the wing due to the fact that the flap flow adheres to the surface.

(3) It is best to use a two branch nozzle for a small aspect ratio flap. The next best is a single nozzle. In case the aspect ratio of the flap is not too small, a single nozzle may be chosen. d_n should not be larger than 5% C_f and h_n should be about 1 d_n. θ_n should be larger than 0. The position of x_n should be determined by the overall arrangement of the aircraft. Λ_n should be larger when the nozzle is located toward the front; e.g., $20^\circ \sim 30^\circ$. When the nozzle is located toward the rear, Λ_n should be smaller, e.g., 10°. When a contracting nozzle is used, supercritical flow is created.

(4) In this work, lift increment of over 20% was realized in the C_μ range (0.012~0.015) of current engines by optimizing the nozzle. It is estimated that the gliding distance of an aircraft upon landing can be reduced by approximately 1/3, which is similar to the lift increase effect of the blown flap. Because of advantages of SWBF such as simple structure, light weight, no need to take up internal space and rugidity, this technique already has its practical value based on the progress made in SWBF research. It may become a promising dynamic lift boosting method to be chosen in aircraft design.

(5) The lift increase efficiency of a blown flap is higher than that of SWBF. After $C_\mu > 0.01$, however, lift no longer increases in the former case.

(6) SWBF may be used to replace blown flaps. On aircraft

requiring relatively small amounts of air, SWBF can be
implemented on single seam retracting flaps[3]. Moving flaps are
widely used in modern fighter designs. The amount of space in
the wing is getting tighter by the day. Thus, using SWBF to
boost lift is more attractive. The research on combustion gas
SWB can free this technique from the limitation of the amount of
air required.

References

[1] Tian Xueshi, Comments on Spanwise Blowing, Journal of
     Aerodynamics, Vol. 4, 1982.

[2] Dixon, C.J., Lift and control augmentation by spanwise
     blowing over trailing edge flaps and control surfaces,
     AIAA paper, NO 72-781, (1972).

[3] Jonah Ottensoser, Subsonic aerodynamic characteristics of
     the T-2C aircraft with spanwise blowing over the wing
     flaps, AD A 033586, (1973).

[4] Cornish, J.J., High lift applications of spanwise blowing,
     ICAS paper, NO. 70-09, (1970).

Characteristics of Three-dimensional Turbulent Boundary Layers

at Low and Subsonic Speeds Measured by a Straight Wing Erected

on a Flat Plate

Xin Dingding, Deng Xueying, Chen Yanqing, Wang Chaoan

(Beijing Institute of Aeronautics and Astronautics)

Abstract

This paper introduces the measurement of three-dimensional
turbulent boundary layer behavior in the attached flow region on
a straight wing erected on a flat plate at low and subsonic
speeds. It also discusses the effects of pressure gradient and
streamline curvature on the laws wall and wake, turbulent stress,
and mixed-length distribution.

The results showed that the Coles velocity model and mixed-
length distribution law which are suitable for a two-dimensional
boundary layer must not be used in three-dimensional cases unless
effects of pressure gradient and streamline curvature are taken
into account. Qualitatively, the subsonic characteristics of the
three-dimensional turbulent boundary layer measured in this work
are not significantly different from those at low speeds.

I. Introduction

The three-dimensional boundary layer is a very frequently
encountered and difficult problem in practice. Due to the fact
that both flow velocity and flow direction perpendicular to the

wall vary, and the latter also causes changes in the structure of the turbulence, it is far more complicated than two-dimensional turbulent boundary layer.

In the past decade, there were many activities in the study of three-dimensional turbulent boundary layers. However, due to the fact that the mechanism to create the turbulence is still not yet clear, there is not a single popular turbulence model to be used to describe the changes of flow parameters in various boundary layers. In addition, because there are very few useful experimental data (even fewer data taken at high speeds), we can only use semi-empirical two-dimensional formulas and experimental curves such as Coles velocity model and Klebanoff mixed-length curve as ancillary equations when we perform three-dimensional calculations. In order to determine the applicability of this type of approximation in computation, we measured the low and subsonic speed three-dimensional turbulent boundary layers with a straight wing erected on a flat plate. This model can be considered as a part of a wing-body combination. Thick wings can be used to enhance the effect of streamline curvature and negative pressure gradient to intensify the flow separation near the wing (See Figure 1). The three-dimensional turbulent boundary layer characteristics in the attached flow prior to separation are discussed in this paper.

Similar studies include: L.F. East [1] measured the mean velocity distribution in the three-dimensional boundary layer of the attached low speed flow of a straight wing erected on a flat plate, and R. Dechow[2] et al measured the mean velocity and

turbulent stress distribution along a low speed streamline of a circular cylinder erected on a flat plate. The model used in this work is identical to that used in reference [1]. But, the number of measurements on subsonic situations as well as on the turbulence were increased. Moreover, all points of measurement are not on the same streamline. Hence it is possible to investigate the effects of pressure gradient and streamline curvature on the data.

/367

(a)   (b)

Figure 1. Oil Flow Pattern on the Flat Plate Around the Airfoil Model

    (a) at low speed (b) at subsonic speed

    1. primary separation line
    2. secondary separation line
    3. model
    4. primary separation line
    5. secondary separation line
    6. model

II. Experimental Conditions

The low speed experiment was completed in the D-2 open loop wind tunnel at Beijing Institute of Aeronautics and Astronautics. When the wind speed is 16m/s, the degree of turbulence in the center of the flow field is $\leq 0.5\%$. the non-uniformity of pressure is $|\Delta q/q| < 0.7\%$ and the deviation of flow direction is $< 0.5^{\circ}$. In this case, the unit length Reynolds number is approximately $10^6 1/m$. The subsonic speed experiment was completed in the experimental section in the G-3 subsonic-transonic wind tunnel at Beijing Institute of Aeronautics and Astronautics. On both sides of the inlet, there are 1cm wide boundary layer channels. When $M_{\infty}= 0.4$, 0.6 and 0.8, the degree of turbulence is $< 1\%$ (including temperature pulsing effect). The maximum inhomogenuity of M, $|\Delta M|_{max}$ is < 0.005. At this time, the unit length Re number is between $10^7 \sim 2 \times 10^7$.
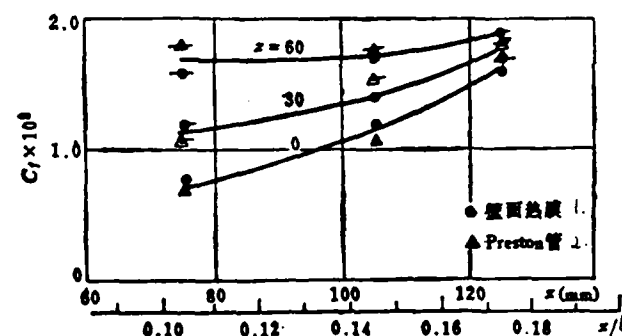

Figure 2. Variation of Low Speed Friction Coefficient Along x-direction

1. thermal wall film
2. preston tube

The airfoil erected on the flat plate is similar in shape as the one used by L.F. East[1] (See Figure 1). Its relative thickness is 25%. At low speeds, the flat plate was installed parallel to the axis of the wind tunnel 22cm from the lower wall surface. The two-dimensional airfoil was placed between the plate and the upper wall of the wind tunnel. In subsonic experiments, the two-dimensional airfoil was placed between the two side walls of the tunnel and one of them was used as the flat plate for measurement. Near the leading edge of the flat plate, there is a 1.5mm diameter trip wire adhered to it to make sure turbulent boundary layer exists on the flat plate. /368

When we measured the mean flow velocity in the boundary layer, total pressure was measured by a pressure probe on a two or three hole direction probe, and static pressure was determined by the static pressure hole on the flat plate surface (or plate surface). The skin friction stress τ_w was determined by a Preston tube. At low speeds, skin thermal film (See Figure 2) was used. At subsonic speeds, Van Driest[3] formula was used (See Figure 3) to prove the feasibility of using a Preston tube. The separation region on the flat plate was determined by oil flow experiments (See Figure 1). Flow temperature and wall temperature were by using thermocouples. The turbulence inside the boundary layer was obtained by using a thermal wire (film) probe and its corresponding display instruments. All necessary data was collected by a data collector and then processed by a Model DJS-130 computer to obtain all the experimental results.
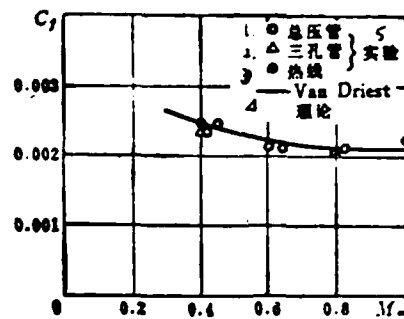
Figure 3. Subsonic Skin Friction Coefficients Obtained by
Various Ways

        1.   total pressure tube
        2.   three hole tube
        3.   hot line
        4.   Van Driest theory
        5.   experiment

During the experiment, the probe was installed on a
traveling mechanism. During blowing, the probe could move up and
down in the direction perpendicular to the flat plate (y-
direction). It could also rotate around the $\tilde{y}$ axis which goes
through the point of measurement. The minimum readings are
0.01mm and $0.1°$, respectively. When measuring turbulence, an "x"
shaped thermal wire probe was first used to measure the velocity
components u_x and u_z, as well as turbulences $\sqrt{\overline{u_x'^2}}$ and $\sqrt{\overline{u_z'^2}}$. At
this time, the projection of the streamline on the plate, s, is
known (because $\beta = \text{tg}^{-1} u_x/u_z$, see Figure 4). It is possible to
obtain the turbulent transient stress $\tau_t = -\overline{\rho u_s' u_y'}$ in the s-
direction by measuring the turbulence $\sqrt{\overline{u_y'^2}}$ and a relevant

28

quantity $\overline{u'_s u'_y}$. In Figure 4, (x, y, z) is the wind tunnel

coordinate. $(\tilde{x}, \tilde{y}, \tilde{z})$ is a coordinate system in which $\tilde{x}$ points

at the direction of flow at the outer fringe of the boundary

layer and $\tilde{y}$ is perpendicular to the flat plate. (s, y, n) is a

boundary layer inner flow direction coordinate system. u_x, $u_{\tilde{x}}$,

$u_s...,u_n$ use the velocity components on the corresponding axes.

$\alpha = (\overline{ox}, \overline{o\tilde{x}})$, and $\beta = (\overline{o\tilde{x}}, \overline{os})$.

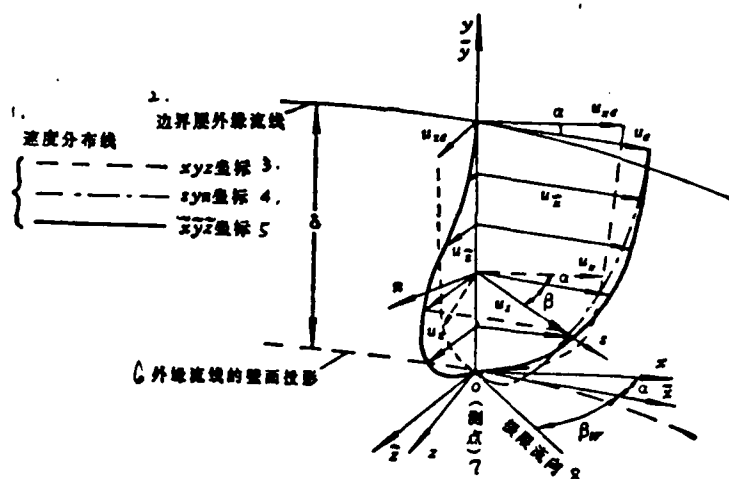Figure 4. Coordinates and Mean Velocity Distribution

        1.   velocity distribution line
        2.   boundary layer outer fringe streamline
        3.   xyz coordinate
        4.   syn coordinate
        5.   xyz coordinate
        6.   projection of outer fringe streamline on the wall
        7.   measuring point
        8.   limiting flow direction

At subsonic speeds, the output signal from the thermal wire represents the product of density ρ and velocity u. With regard to the mean velocity and turbulence, the effect of ρ can be eliminated in approximation through calculation. As for tangent turbulent stress, it is only possible to adopt a mass weighted model[4] to express the pulse related term which is defined as

$$(\overline{u_x' u_y'})_\rho = \frac{\overline{(\rho u_x)'(\rho u_y)'}}{\bar{\rho}^2}$$ (A)

The positions of the measuring points are shown in Figure 5. There are 9 low speed points and 4 subsonic points. They are all located in the attached region in front of the separation line.

Figure 5. Experimental Model and Measuring Stations

30

      (a) at low speed   (b) at subsonic speed

1. straight wing
2. measuring station
3. flat plate
4. separation line
5. trip line
6. leading edge of flat plate
7. measuring station
8. separation line
9. wing model

III. Discussion of Experimental Results

In order to verify that the flat plate boundary layer flow is two-dimensional when the straight wing is not erected, the two-dimensional turbulent boundary at low or subsonic speed was first measured. After adding a "wake function" expressed by $W=W(y/\delta)$ to the right of the "wall law", equation (1) can be extended to the outer area of the boundary layer. If Coles' velocity distribution law[6] is used to determine this "wake Function", then

$$\frac{u}{u_\tau} = A\ln\left(\frac{yu_\tau}{v}\right) + B \approx 2.44\ln\left(\frac{yu_\tau}{v}\right) + 4.9 \tag{1}$$

$$\frac{u}{u_\tau} = A\ln\left(\frac{yu_\tau}{v}\right) + B + [A\Pi(x)]\left[2\sin^2\left(\frac{\pi}{2}\cdot\frac{y}{\delta}\right)\right] \tag{2}$$

For a flat plate, if Re_θ defined by the momentum thickness is /370 5000, then $\Pi(x)=0.55$[4]. The results at low speeds agree with the above formula well (See Figure 6, flat plate curve). At this time, $A \approx 1/k$ where k = 0.41 (Karman constant). $B \approx 4.9$.
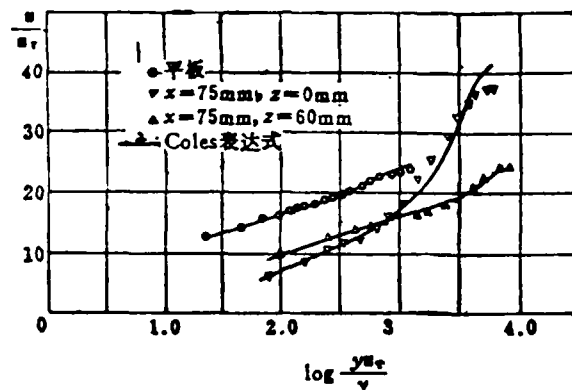
Figure 6. Comparison of Experimental Mean Velocity Distribution to Calculated Mean Velocity Distribution

1. flat plate
2. Coles expression

In two-dimensional subsonic condition, the experimental results are expressed as $\frac{u_e^* - u^*}{u_\tau} = f\left(\frac{y}{\delta}\right)$ according to the velocity defect law (See Figure 7), where u* is the Van Driest generalized velocity[4,5]. In the figure, the defect law profile based on the Coles velocity distribution is also plotted. They are in very good agreement.
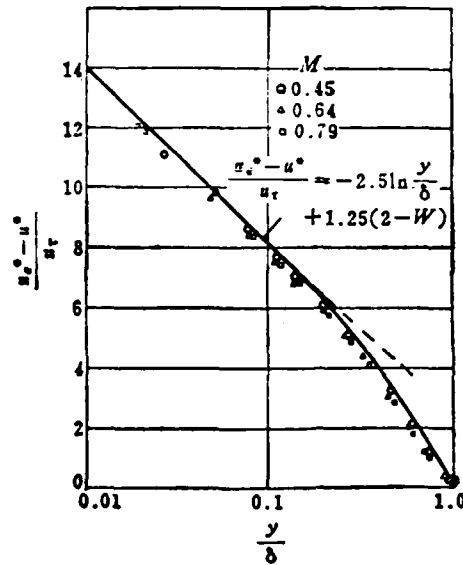
32

Figure 7.   Generalized Velocity – Defect Law Profile at Subsonic
            Speed

Comparing the results at $M_\infty = 0.4$ with a flat plate and

Klebanoff's experiment at low speed [7] (See Figure 8), we can

see that the trend of change is similar. The numerical

differences are caused by different turbulence structure in the
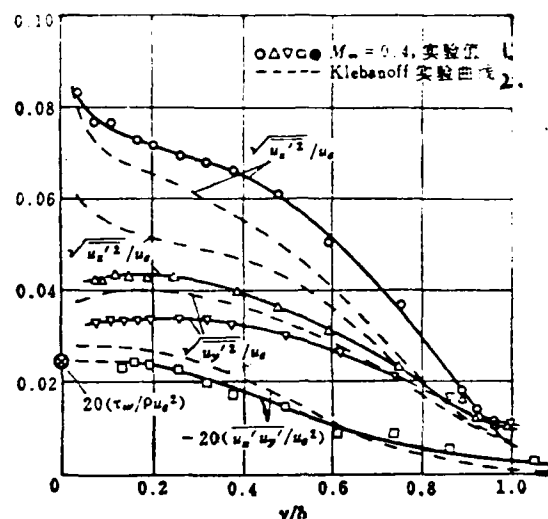
wind tunnel.

33

Figure 8. Distribution of Turbulence on the Flat Plate at $M_\infty = 0.4$

1. experimental values at $M_\infty = 0.4$
2. experimental curve obtained by Klebanoff

If the three-dimensional mean velocity distribution is expressed by the Cole velocity model, then constants such as A, B and Π in equation (2) should be determined by three-dimensional experiment. In this case, we use u_s to replace u. (Coles took u as the component in the tangential stress direction along the wall surface. This is essentially the same as our approach in the inner layer. In the outer layer, however, there are differences. Based on various experimental results [1], it is better to use u_s in the outer layer. Constants such as A, B and Π vary with the point of measurement (See Figures 9 and 10). The flow pressure intensity coefficient and deflection angle are

34

different at each point of measurement (See Figures 11 and 12).
On the x = 75mm line, the back pressure gradient at z=0 is very
high. At z=60mm, the back pressure gradient and streamline
curvature are both large. Based on Figure 6, we can see that the
velocity distribution at those two points does not agree with the
Coles expression curve well. Comparing Figures 9 and 10 to
Figures 11 and 12, we found that the three-dimensional effect is
high. (The streamline curvature is large. Based on experimental
results we know that when α is large β_w is also large (See Figure
4). This indicates that when the angle of deviation of the outer
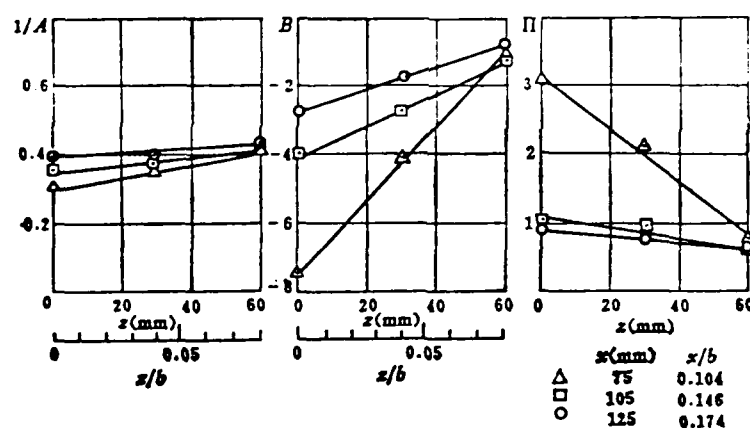fringe is large, the streamline curvature is also large.)

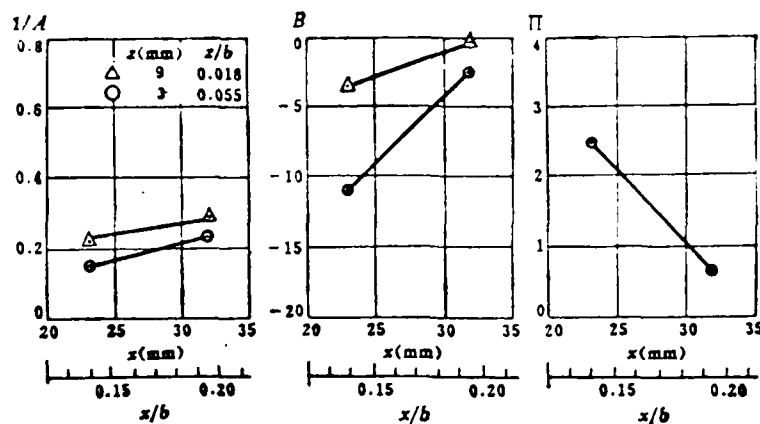Figure 9. Variation of Coefficients A, B and Π at Low Speed

35

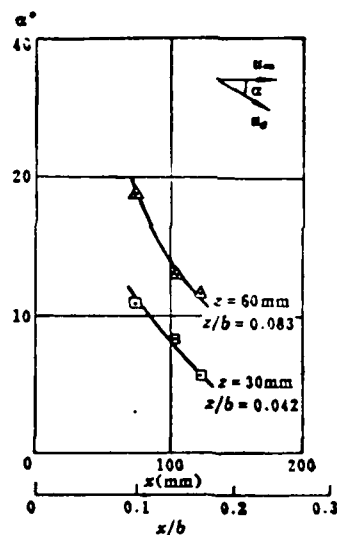Figure 10.   Variation of Coefficients A, B and Π at $M_\infty = 0.4$

Figure 11.   Pressure Coefficient Variation along x-direction at Various z positions
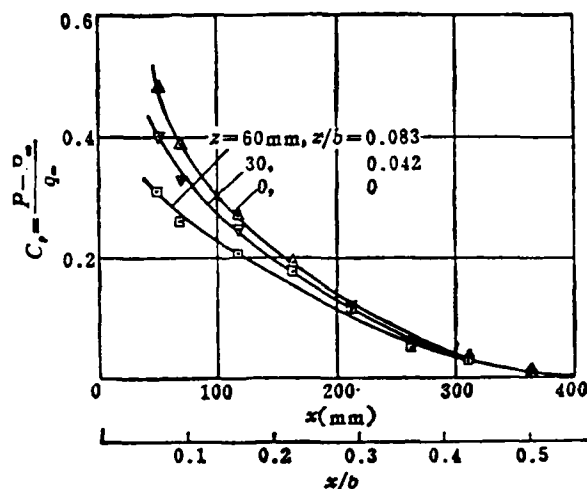
Figure 12.   Variation of Flow Angle at the Edge of Boundary
Layer along x-direction

The higher the back pressure gradient is, the larger the
values of A, B and Π deviate from their two-dimensional flat
plate values. At the same point of measurement, three-
dimensional effect and pressure gradient increase with increasing
M. Nevertheless, it was demonstrated experimentally that A and B
did not vary by much with M. Only Π varied significantly with M
(See Figure 13). With regard to the relation between velocity
components $u_{\tilde{x}}$ and $u_{\tilde{z}}$ in the boundary layer, it was experimentally
shown that they are essentially in a triangular distribution; in
agreement with Johnston's transversal velocity distribution
pattern[8].

Based on the curve shown in Figure 14, when the value of x
remains the same, the curvature of the streamline increases with
increasing z. (Three dimensional effect is enhanced. In this
case, the back pressure gradient varies slightly.)

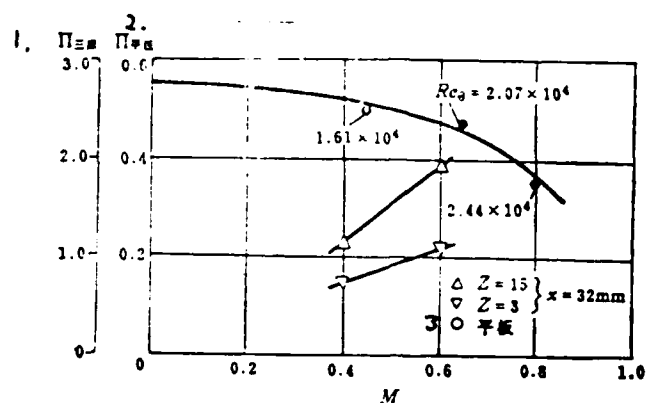Figure 13.   Variation of Two-dimensional and three-dimensional
             Turbulent Boundary Layer Coefficients Π with Re_θ
             and M_∞

         1. $\Pi_{\text{three-dimensional}}$

         2. $\Pi_{\text{flat plate}}$

         3. flat plate

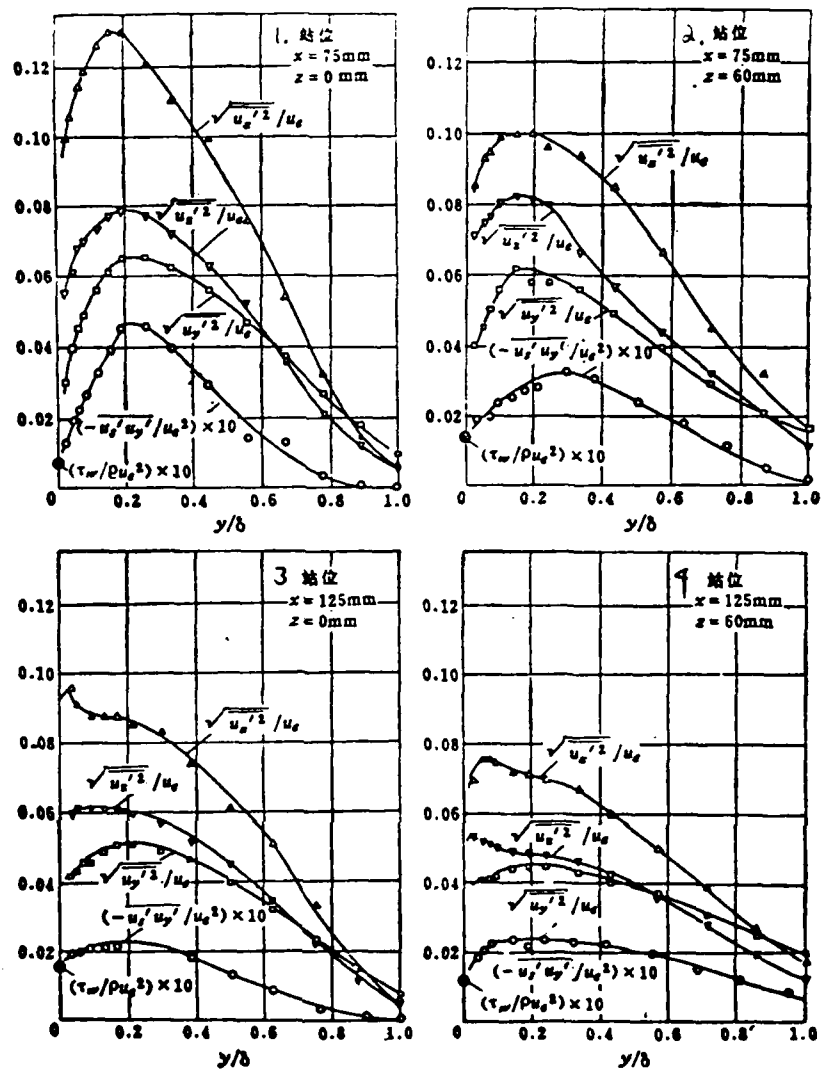Figure 14.   Experimental Turbulence and Turbulent Shear Stress
             Distributions Measured at Low Speed at Various
             Stations

             1.   station
             2.   station
             3.   station
             4.   station

The curve becomes flatter, indicating that the turbulence is diffused by the three-dimensional flow. It is difficult to form a peak. At fixed z, the back-pressure gradient decreases with x. The peak moves away from the flat plate. Furthermore, its value increases.

From the turbulent stress $-\overline{u'_s u'_y}/u_e^2$ curve, we can see that the curve is linear near the plate surface. This is because the velocity near the wall is close to zero. The momentum equation along the streamline is

$$\frac{\partial p}{\partial s} \approx \frac{\partial \tau}{\partial y} \qquad (3)$$

As long as $\partial p/\partial y \approx 0$ in the boundary layer, then $\tau \partial/\partial y = $ constant, which means the turbulent stress varies linearly. In the bottom viscid layer, $\tau = \tau_1$. Because the bottom viscid layer and transition layer are very thin ($<2\%\delta$), it can be considered as wall friction $\tau_w \approx \tau_1/$bottom layer$\approx \tau_f$/transition layer. This point has been verified experimentally. The value of $\tau_w/\rho u_e^2$ measured by a Preston tube or a wall thermal film is very close to the extrapolated value from $\dfrac{-\overline{u'_s u'_y}}{u_e^2}$ This also indicates that the experimental results are reliable.
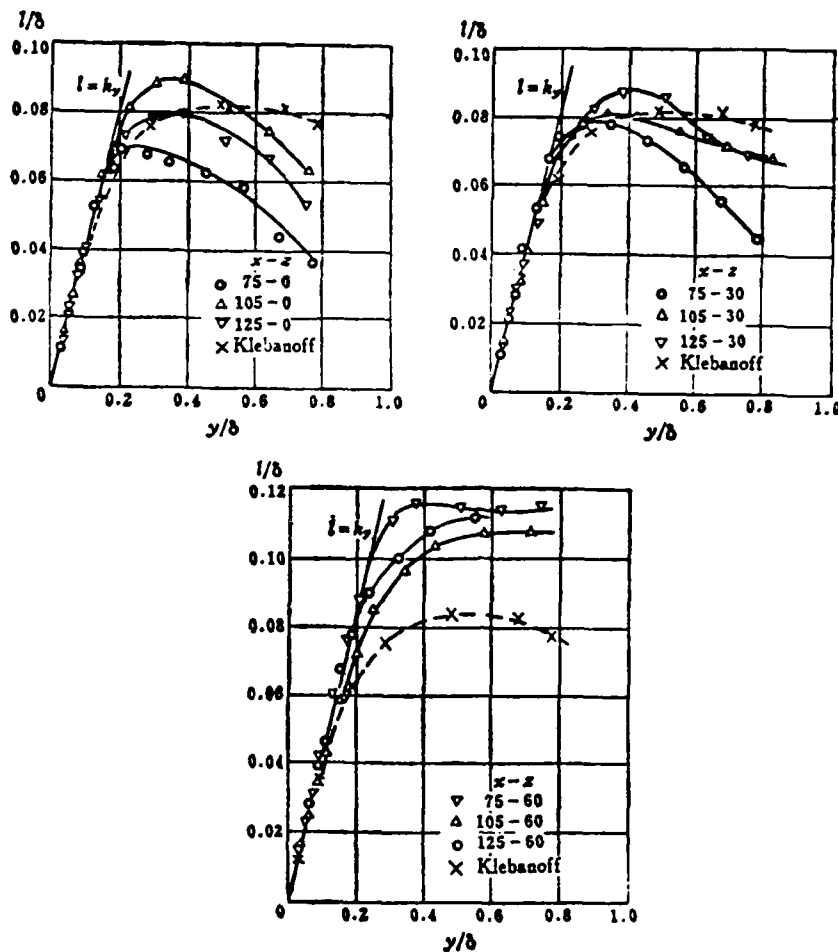
Figure 15.   Mixing-length Distribution at Various Stations at
             Low Speed

If we use the mixing length concept to express τ_t as $\tau_t = l^2$ $\left(\frac{\partial u}{\partial y}\right)^2 \rho$, and let $l = k_y$. then it is possible to prove that the following relation exists when there is a pressure gradient [9].

$$\frac{u}{u_\tau} = \frac{1}{k}\left[\ln\left(\frac{yu_\tau}{\nu}\right) + B + \frac{1}{2}\ \frac{\nu}{\rho u_\tau^3}\ \frac{\partial p}{\partial s}\left(\frac{yu_\tau}{\nu}\right)\right] \tag{4}$$

41

Comparing the above equation to equation (2), in the inner region of a three-dimensional turbulent boundary layer (in this case the third term of the right side of equation (2) can be omitted) when $\frac{\partial p}{\partial s} > 0$, $1/A < k$. This means that the larger the back pressure gradient is, the smaller $1/A$ becomes. The experimental results also confirmed this point (See Figure 9).

Based on the definition of the turbulent mixing length $\frac{l}{\delta} = \frac{(-u_x' u_y')^{1/2}}{\left(du_x/ d\left(\frac{y}{\delta}\right)\right)}$, the $1/\delta$ vs y/δ curve was obtained (See Figures 15 and 16). We can see that the curve gradually becomes linear in the region $y/\delta < 0.2$ and its slope is $\approx k$. A careful observation revealed that the slope decreases slightly with increasing back pressure gradient. With increasing streamline curvature, the mixing length rises to its maximum value. Figure 16 shows the $l/\delta = f(y/\delta)$ curve in the turbulent boundary layer of the flat plate at $M_\infty = 0.4$. As compared to the curve at low speed, the slope does not vary much. However, the maximum value increases. Figure 17 shows the variation of $\frac{\sqrt{u_x'^2}}{u_e}$, $\frac{\sqrt{u_z'^2}}{u_e}$ and the mass weighted correlation of the turbulent stress $\overline{u_x' u_z'}/u_e^2$ p vs y/δ at subsonic speed at the station x=32mm and z=15mm. It is obvious that the subsonic characteristics of the three-dimensional turbulent boundary layer are essentially the same as those at low speed. The effect of numerical compressibility still remains to be investigated.
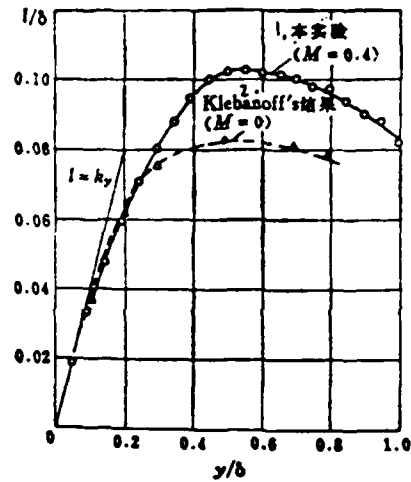
42

Figure 16.   Comparison of Mixing Length Distribution in the
Turbulent Boundary Layer of the Flat Plate at
$M_\infty = 0.4$ to that at Low Speed
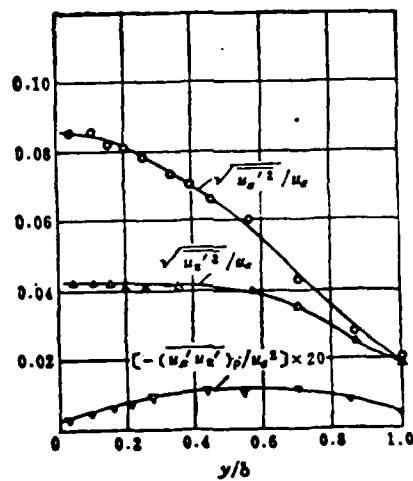
1.   this experiment
2.   Klebanoff's result

Figure 17.   Normal Distribution of Turbulent Values in Station
x=32mm and z=15mm at $M_\infty = 0.4$

1. A conventional probe such as a total pressure tube, or a
two or three branch directivity probe can be used to determine
the average speed and flow direction in a three-dimensional
turbulent boundary layer. It is possible to use a Preston tube
to measure the frictional stress on the wall. Its value is in
basic agreement with the extrapolated value based on thermal film
or thermal wire measurement. An "x"-shaped double wire probe can
be used to measure the turbulence and turbulent shear stress.
The two-dimensional results agree with those obtained by other
researchers.

2. The use of wall law and wake law suitable for a two-
dimensional turbulent boundary layer, such as using Coles
velocity mode to express the mean velocity distribution in a
three-dimensional boundary layer, is appropriate only when the
pressure gradient and streamline curvature are not too large.
The coefficients A, B and Π vary with varying pressure gradient
and streamline curvature. At subsonic speed, the effect of M on
the velocity distribution curve can be eliminated by using Van
Driest generalized velocity $u*$[5] to replace the real velocity.

3. The turbulence and the normal distribution of the
turbulent shear stress of a three-dimensional turbulent boundary
layer are similar to those in the two-dimensional case. However,
as the pressure gradient increases, the distribution curve shows
a peak. In addition, the peak has a tendency to move outward.
As the curvature of the streamline increases, the contour becomes
flatter.

4. The distribution of mixing length in a three-dimensional

44

turbulent boundary layer does not remain unchanged. Instead, it increases with increasing pressure gradient. The slope of the straight line section of the curve in the inner boundary layer region decreases slightly. As the curvature of streamline increases, the maximum mixing length also rises.

5. There is no substantial difference between the experimentally measured subsonic characteristics and the low speed characteristics of a three-dimensional turbulent boundary layer. This aspect still requires further investigation.

References

[1] East, L.F., and Hoxey, R.P., "Low-speed Three-Dimensional Turbulent Boundary Data" ARC R & M 3655, March (1969).

[2] Dechow, R. and Felsh, K.O., "Measurements of the Mean Velocity and of the Reynolds Stress Tensor in a Three-Dimensional Turbulent Boundary Induced by a Cylinder Standing on a Flat Wall." DEFE 77. Universitat Karlsruhe. (1977).

[3] Hopkins, E.J., and Inouye, M., "An Evaluation of Theories for Perdicting Turbulent Skin Friction and Heat Transfer on Flat Plates at Supersonic and Hypersonic Mach Numbers" AIAA J., Vol. 9, No. 6, pp 993-1003, (1971).

[4]   Cebeci, T., and Smith, A.M.O., "Analysis of Turbulent
      Boundary Layers" Academic Press, (1974).

[5]   Van Driest, E.R., "Turbulent Boundary LAyer in Compressible
      Fluids" J. Aeronaut. Sci. 18, 145.

[6]   Coles, D.E., "The Law of the Wake in the Turbulent Boundary
      Layer" JFM, Vol. 1, pp 191-226, (1956).

[7]   Klebanoff, P.S., "Characteristics of Turbulence in a
      Boundary Layer with Zero Pressure Gradient" NACA TN-3178,
      (1954).

[8]   Johnston, J.P., "On the Three-Dimensional Turbulent Boundary
      Layer Generated by Secondary Flow" ASME Journal of Basic
      Engineer, Vol. 82, March pp. 233-248, (1960).

[9]   Berg, B. van den, "A Three Dimensional Law of the Wall for
      Turbulent Shear Flows" JFM, Vol. 70, July pp. 149-160,
      (1975).

Study of A Multi-color Flow Field Survey Technique

Harbin Aerodynamics Research Institute

Helian Huizheng, Xiao Rongduan, Zhang Xiaodi, Jia Juntong,

and Bian Xiaoxian

Abstract

A fast and easy multi-color flow field survey technique with 8 colors and 15 details is introduced in this paper. A fast responding total pressure probe is used to perform high density scanning of different cross-sections of the flow field in order to acquire a color pattern of the flow field showing various isoparameters (such as isobar, isotherm ......) in different colors. This can facilitate the study of three-dimensional flow.

This paper deals with major problems encountered in the development of equipment required in this technique. Recently obtained experimental results are also presented. The special features of this technique and its possible range of applications are also discussed.

Introduction

In studying the aerodynamic topology of an aircraft and aerodynamic characteristics at large attack angles, observation of the spatial flow field surrounding the model is extremely important. Observation of the flow field in a wind tunnel experiment, however, is very complicated. On one hand, a great

47

deal of data must be collected in a three-dimensional space. On the other hand, it is not easy to clearly describe the spatial flow field structure based on these data.

The recently developed "color flow field survey" technique provides an effective means to solve the above problem. Figure 1 is a photograph taken by using a recently developed color flow field survey technique which shows the flow field of a canard vortex on a cross-section over the wing. The profile of the canard vortex and the wing vortex, as well as their relative position, are vividly displayed.

This technique is an extension of the LED technique used by the Beijing Aerodynamic Laboratory in the U.S. In order to explain this development, the Boeing technique is briefly introduced in this paper. Then, our effort in expanding multi-color light sources will be described. Finally, some observations are reported and potential benefits of this technique are also identified.

I. Basic Method and Its Discussion

In 1980, J.P. Crowder of Boeing Aerodynamic Laboratory used LED to obtain a color flow field pattern in the wind tunnel for the first time[1]. He placed a series of LEDs capable of emitting red, green and yellow light at the end of a total pressure probe. It was connected to a signal processing device outside the tunnel. The probe scanned the flow field. Different pressure signals triggered different colors to expose the

negative to obtain various iso-parameter distributions of the flow field by different color spots. This technique was first used by us in 1982 in the FL-5 wind tunnel[2], as shown in Figure 2.
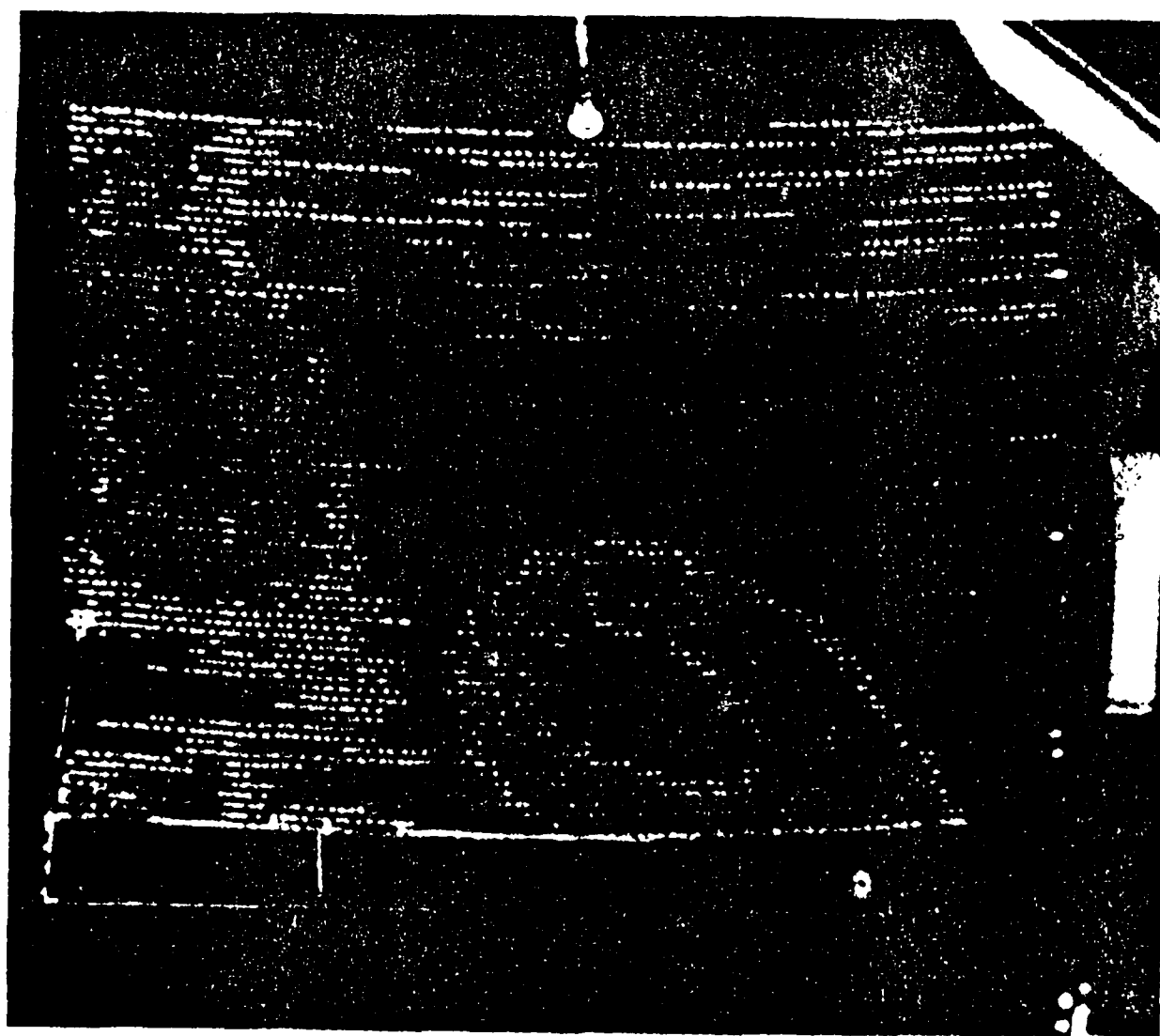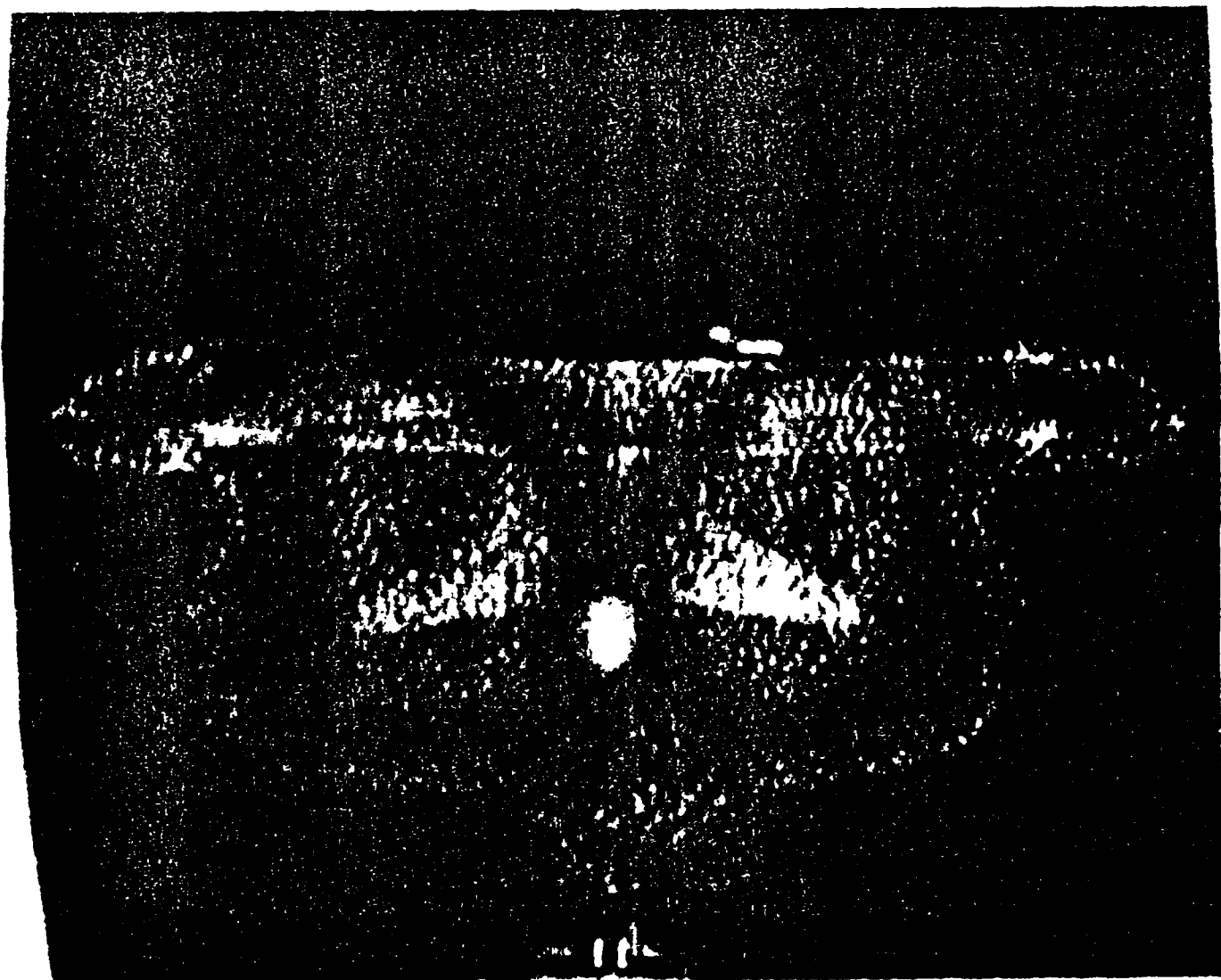

FIGURE 1. Canard Vortex Passing Over The Wing.

FIGURE 9. Full Wake Image of Figure A at Maximum Lift Coefficient
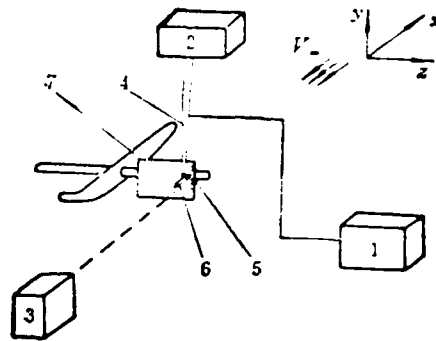
Figure 2. The Colour Visualization of Flow Field with Technique
of LED

1. signal
2. scanner
3. camera
4. probe support
5. pressure probe
6. light-emitting diode (LED)
7. searched plane

The Boeing method employed small volume (Φ4 x 8), fast response (below microsecond) LEDs to realize the real place (next to the probe) real time conversion from pressure signals to color signals. Nevertheless, it could only form colors, i.e., red, green, yellow, (mixing red and green) and black (when the LED is not lit). There are difficulties in the simultaneous visualization of the overall profile as well as the details of the flow field. Because vortex field ranges from the free flow region to the center of the vortex, the flow field parameters may vary widely. This is particularly true at large angles of attack. Due to the fact that only a few colors are available to cover the entire flow field, the difference represented by each color is very large. Furthermore, the signal in the same range shows up in the same color. It is impossible to identify the fluctuation of the flow field in this range. Hence, the resolution of the variation of a parameter with position in the flow field is not high in the graph. The key to improving this technique is to develop more colors and to refine the range covered by each color to raise the resolution of the pattern.

It was also discovered in studying the Boeing method that in a steady flow field with spatial parametric variations, the signals detected by the probe are also time dependent because the probe scans through the flow field, i.e.,

$$\frac{dP}{dt} = \frac{dP(s)}{ds} \cdot \frac{ds}{dt} = \frac{dP(s)}{ds} V \qquad \text{(A)}$$

where dP/dt - rate of change of the signal detected by the probe
                    with time,

dP(s)/ds - gradient of flow field parameter (in the

s-direction along the scanning track),

ds/dt - scanning rate of the probe (equal to a constant).

It is obvious that $dP/dt \neq 0$. The system operates in a non-static state. Hence, it is necessary to consider the frequency response of the system. From the viewpoint of the system structure, the frequency response of the primary signal detecting component consisting of the "probe-pressure transmitting-sensor" is lower than that of the electrical circuit and optical system. Improper selection may lead to significant distortion of the signal. Figure 3 shows the total pressure signal distribution along scanning trajectory in a certain vortex field using two different methods. Curve A represents the average value of the scanning record of the low frequency response primary signal detection system. By comparing them we can see the distortions in amplitude and phase. When the frequency response of the detection system is too low, the quality of the pattern will be seriously affected. Otherwise, it is necessary to significantly reduce the scan speed. It is inappropriate to reduce the scan speed for a large flow field.
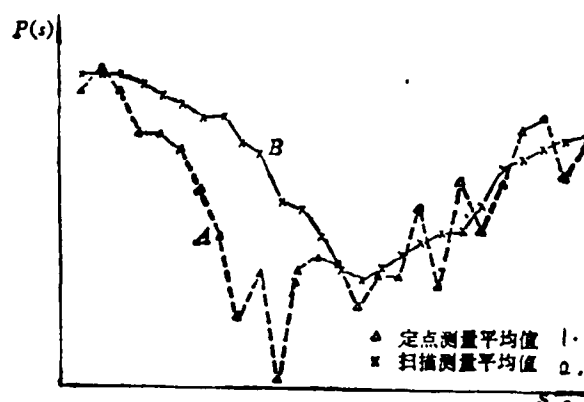
P(s)

B

A

定点测量平均值 1.
扫描测量平均值 2.

s

Figure 3. Comparison Between Data from Fixed Point Measurement
and Results Obtained from Scanning by Primary System
of Low Frequency Response

1. average value of fixed point measurement
2. average value of scanning measurement

II. Multi-color Visualization and Its System Formation

The light source we are seeking must be able to provide many
colors. Furthermore, its volume must be very small (to be able
to operate in the wind tunnel). It also must have fast response.
To this end, we designed a multi-color light source and its
transmission system to successfully replace the original LED.
The number of colors is increased to eight and the identifiable
signal regions are increased to fifteen.

The black diagram of this system is shown in Figure 4. Its
operating principle is briefly shown as follows:

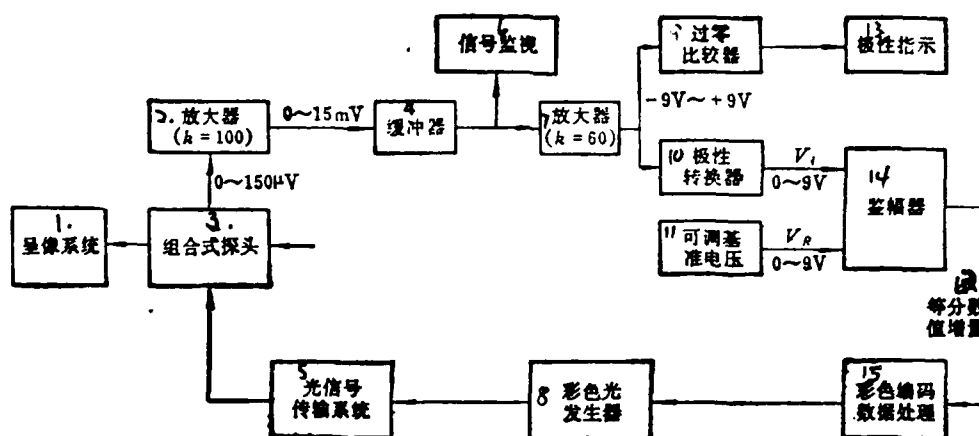Figure 4.   Block Diagram of Signal Processing System

1.   imaging system
2.   amplifier (k=100)
3.   composite probe
4.   buffer
5.   optical signal transmission system
6.   signal monitor
7.   amplifier (k=60)
8.   color light generator
9.   zero comparator
10.   polarity converter
11.   adjustable bias
12.   equal fraction increment
13.   polarity indicator
14.   amplitude detector
15.   color code data processing

When the probe scans across the flow field, the transducer sends out a series of continuously varying voltage signals (analog). After getting amplified, the signal is sent into the zero comparator and the voltage polarity converter. After the absolute value of the signal is taken, it is sent into the amplitude comparator with a series of adjustable bias voltages. The output is in the form of equal fraction increments. After decoding and coding processes, binary signals of the three basic colors, i.e., red, green and blue, are generated to control the color and brightness of the multi-color optical signal generator. Various colors corresponding to the signals are generated. Through the use of a specially designed optical device, the optical signal is fed to the rear of the probe in the tunnel to form a light spot which moves together with the probe. The color of the light spot depends on the magnitude of the signal detected by the probe. The probe scans through the observation plane in the flow field at a high density with a very small line spacing (approximately 3mm). Spatial distribution of the pressure signal is displayed by light spots which continuously change in color /381 and position. They are recorded on film, resulting in the final result shown in Figure 1.

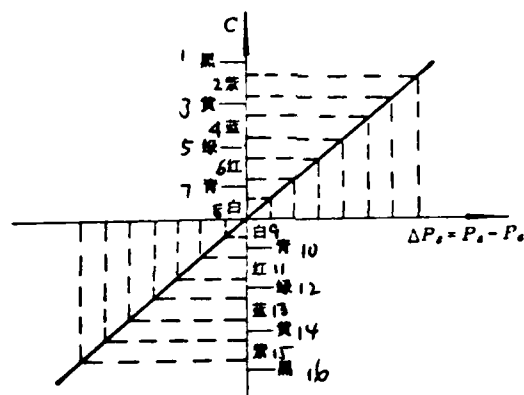Figure 5. Relationship Between Pressure Signal and Color

        1. black
        2. violet
        3. yellow
        4. blue
        5. green
        6. red
        7. blue green
        8. white
        9. white
       10. blue green
       11. red
       12. green
       13. blue
       14. yellow
       15. violet
       16. black

The colors provided by this type of light source increase
from the original red, yellow, green and black to eight colors
including white, blue green, red, green, blue, yellowish violet
and black. The relation between the sequence of color and signal
variation is shown in Figure 5. Experimental results proved that
this kind of arrangement of distinctive difference between
neighboring colors is better than the flow field pattern
according to an arrangement based on wavelength[3].

As shown in Figure 6, signals of the same absolute value and
opposite sign use the same color. With respect to the displayed
object (which is the spatial distribution of the total pressure
of the flow field), it is continuous. An equi-parameter region
is always enclosed by the free flow field and terminated at the
surface. Hence, there is no confusion in pattern recognition
using this technique. On the contrary, there are tremendous
advantages. The number of equi-parametric regions in the flow
field displayed is almost doubled as compared to the number of
colors of the light source. It becomes the 8 color 15 region
pattern such as the one shown in Figure 5; i.e., black-violet-
yellow-blue-green-red-blue green-white-blue-green-red-green-blue-
yellow-violet-black. Of course, the sign of a signal is relative
to a specific reference. Presently, we are detecting the total
pressure signal. The reference is the atmospheric pressure
outside the tunnel during the experiment. (In an open wind
tunnel, it is the static pressure of the free flow.) It is
introduced into the reference chamber of the pressure
differential transducer as the basis for zero pressure.

A compound total pressure probe was designed to improve the dynamic characteristics of the primary signal detection system, as shown in Figure 6. The probe is composed of a total pressure tube with a flow regulating jacket, a Model PDCR-42 pressure transducer and an optical signal display point. Its characteristic frequency was determined to be around 1 kc.

We referred to the flow regulating concept of the Kiel tube to include holes on the side in order to increase the range of insensitivity of the probe to the direction of the flow. It was proven to be comparable to that of the kiel tube.
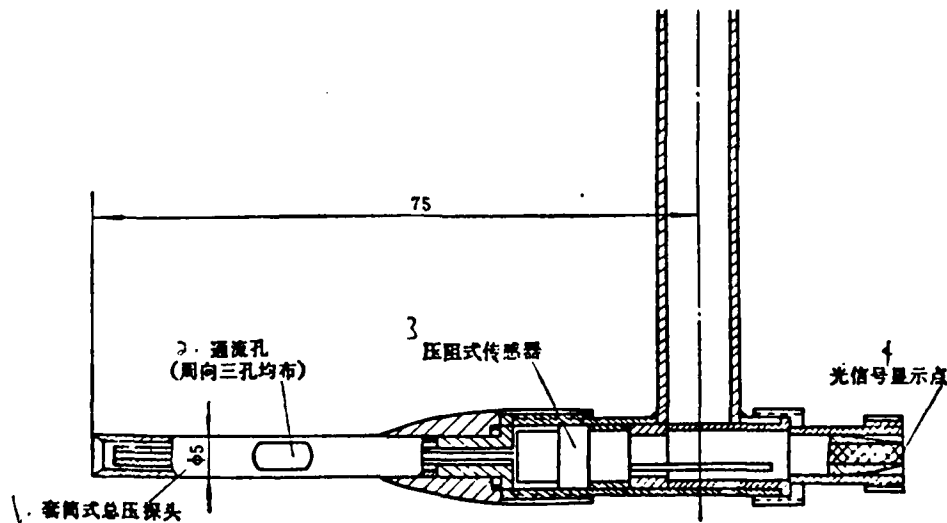

图6　组合式压力探头

Figure 6. Compound Total Pressure Probe

    1. jacket type total pressure probe
    2. flow through holes (3 holes evenly distributed circumferentially)
    3. pressure transducer
    4. optical signal display point

When the system described above is used to survey the average pattern of the vortex field in a low speed wind tunnel, the allowable scan speed reaches 6~8 cm/s. The quality of the flow pattern is good. /382

III. Pattern Analysis and Examples in Applications

This system was used in the high density scanning of the vortex field involving a canard model. Very good results were obtained in visualizing the canard vortex and wing vortex, as well as their natural interference.

1. In the outer region of the vortex, the pattern is mostly in an annular color band structure (See Figure 1), indicating that the total pressure loss at the same radius from the center due to the vortex motion is identical. Consequently, the pattern appears as concentric rings. In particular, when the vortex rolls up and the interference of the wing and fuselage is small, the pattern becomes closer to the situation described above. The canard vortex shown in Figure 1 represents this case.

The outer color ring is violet (corresponding to layer signals as shown in Figure 5). The color gradually changes to yellow, blue, green, red,...... towards the center with decreasing signal magnitude. This reflects the situation that the total pressure loss increases with decreasing radius. Most of the ring patterns are not regular due to the presence of interference. The interference is higher where there is obvious distortion. It is very direct and intuitive.

2. Breakdown of Vortex

By using techniques such as the oil flow pattern we found the following characteristics in flow patterns before and after vortex breakdown: Prior to its breakdown, the outer portion of the flow pattern appears to be in a regular ring structure. The inner part of the pattern is highly irregular. The preliminary viewpoint is that the flow field at the vortex center is highly unsteady. Futhermore, it is extremely sensitive to the introduction of the probe. Thus, it is not possible to record any regular pattern. Both inner and outer part of the vortex pattern are regular after vortex breakdown takes place.

With respect to a complicated vortex field, flow patterns obtained at various cross-sections can be used to describe the structure of vortices in the system and their natural interference. This is very valuable to both theoretical and experimental researchers in aerodynamics. We believe that these patterns will provide evidence for researchers in the following areas:

1. It can be used to determine the presence of vortices, as well as their relative strength and center positions.

2. The overall picture of a three-dimensional flow field can be put together by combining several cross-sectional patterns. The trajectory of the vortex center can also be approximately determined. There is no doubt that this will assist theoretical or computational aerodynamic researchers in determining whether a mathematical model is valid.

3. It can be used to compare the mutual interference among

various components of the aircraft as well as any external attachments.

4.   It can determine the total pressure distribution in the wake region.

5.   Advanced aerodynamic layout of aircraft can be studied   /382 by combining all the above items.

As an example, the entire wake pattern of an F16-A is shown in Figure 7.   The attitude of the model corresponds to the state of maximum lift coefficient.   The position of the cross-section is approximately one tenth of the overall length of the aircraft away from the tail.

IV.   Conclusions

The use of the "color light source transmission system" multi-color flow field survey technique maintains the advantages of similar techniques using LED; i.e., fast, simple and direct.

The resolution of the flow pattern was improved as the number of colors available was increased.   Cross-sectional flow patterns containing a great deal of information can be obtained. It is an effective way to study complicated flow motions.

This technique is not only appropriate for visualizing the pressure field and is not only limited in aerodynamic studies. It can be used in the study of other flow parameters such as velocity field, temperature field and liquid flow field so long as there is a suitable primary signal detection system.

Although attempts were made to miniaturize the probe,

interference still exists in this type of contact measurement. Further improvement is certainly worthwhile pursuing.

References

[1] Crowder, J.P., Hill, E.G. and Pond, C.R., Selected Wind Tunnel Testing Developments at the Boeing Aerodynamics Laboratory, AIAA 80-0458-CP.

[2] Helian Huizheng, Xiao Rongduan and Zhang Xiaodi - A New Flow Visualization Technique - Preliminary Investigation of the "Color Survey Method", Chinese Aerospace Technical Document No. HJB830115, Ministry of Aeronautics, (1983).

[3] Winkelmann, A.E., An Experimental Study of Separated Flow on a Finite Wing, AIAA-81-1882.

Observations on Wake of a Circular Disk During Starting By

Hydrogen Bubble Method

Lian Qixiang

(Beijing Institute of Aeronautics and Astronautics

Abstract

This paper summarizes the flow in the wake region of a circular disk during starting using a hydrogen bubble technique. During starting, a symmetric vortex is formed behind the disk. It gradually grows layers and moves downstream. The size and position of this vortex as a function of time was observed. Its relation with a reverse flow parameter in the wake region was also determined. During the late starting period, the vortex was separated and broken down. Just before its breakdown, the reverse flow velocity reached its maximum, which is approximately 1.3 times of the free flow velocity. During the breakdown process, the wake might sway at large amplitudes.

I. Introduction

Unsteady separation flows are observed in many engineering problems, such as the flows around a building under a gust wind or wave, the process of acceleration or deceleration of a warhead shape body, at the starting stage of a parachute or an ejection seat, etc. There are many types of separation flows and the studies are limited[1,2]. More information is available on the

flow field at the starting edge around a two dimensional
cylinder. In those studies, the initiation of the vortices is
observed by flow field visualization method. Early in the
twenties, Prandtl had observed the starting vortex behind the
cylinder. Recently, Yun Tian-tuo[3], Sarpkaya[4] and Golovkin[5]
and others have carried out observations on the vortices at the
starting stage under steady acceleration or unexpected
acceleration. The separation around a sharp angle is another
type of flow. Pullin[6] have observed the starting vortex around
a two dimensional closed angle. Studies on such unsteady state
separation flow are very few. The flow field around a circular
disk is a typical separation flow on a body having sharp closed
angle, which is similar to the separation flow around a warhead
shape body or a parachute. The separation point on a disk is
fixed at the edge, which is convenient in study. The hydrogen
bubble method is a flow field visualization method developed in
the sixties. It can be used for qualitative observations and to
determine the profile of the flow speed. Since the flow speed at
any point in an unsteady flow field is continuously changing, it
is necessary to determine the flow speeds at many points in a
short moment in order to understand the overall flow and to
establish a flow model. The regular flow meter cannot be used to
satisfy the requirement. The hydrogen bubble method is suitable
to investigate the unsteady flow[7]. It has been widely used in
studying the structure and separation of the turbulent flow. We
have used this method to observe the development of the starting
vortex on circular disks and the reverse flow in the wake.

II. Experimental and the Test Method

The arrangement of the test facilities is shown in Figure 1. Two circular disks with diameters of 8cm and 12cm respectively and thickness of 1mm were used. The cross-sectional area of the water channel was 0.4 x 0.4m^2 and the length was 6.8m. A water pump was used to drive the flow with circulation. Various starting conditions were created by adjusting the power and the cut-off valve. Four starting processes have been studied and the variation of the free stream speed, U, is shown in Figure 2.
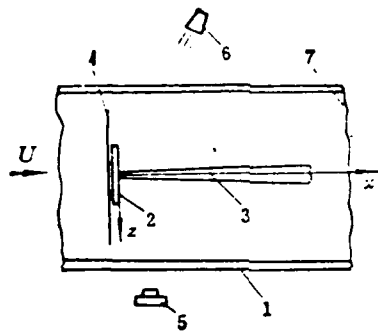
/385

Figure 1   Arrangement of the test facilities

    1. water channel
    2. circular disk
    3. support
    4. platinum wire
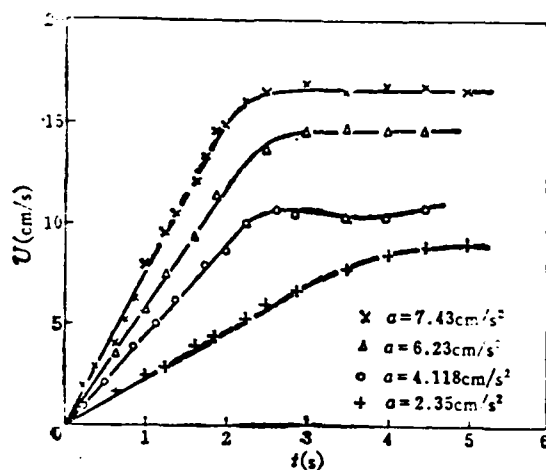   5. camera
    6. lamp
    7. anode

Figure 2. The variation of free stream speed in starting period

Therè was always a rather long period with dU/dt equaling to a constant after starting. U reached a steady value after a short transition period. A platinum wire was installed near the circular disk to investigate the starting vortex as shown in Figure 1. One or more platinum wires were installed in the wake to measure the back flow. The platinum wires were connected electrically to the negative and the positive electrode was installed in the downstream without interference of the flow field. The pulsed power source delivered a rectangular wave with a voltage from 50 to 200 volts and a frequency of 12.6 Hz. The diameter of the platinum wire was 25 µm. The average diameter of the bubbles was about 12.5 µm and time constant for the follow-up ability was about 3 x 10^{-6} sec[7]. The hydrogen bubbles could follow-up the speed momentarily and reached 99.99% of the speed

at a fixed point within 3 x 10^{-5} sec. The hydrogen bubbles generated at the platinum wire formed a line during each electrical pulse. The line formed by the bubbles was the timing line. The flow speed at a fixed location could be determined approximately by dividing the distance, Δs, between the two timing lines by the period of the pulse, Δt. The location, where it had more dense timing lines of hydrogen bubbles in the photograph, had lower flow speed. The flow profile can be measured by the distribution of the hydrogen bubble lines as described in Reference [7,8]. We have made over 6000 photographs using a camera with speeds of 16 and 32 pictures per second to get the flow field data.

III. Test Results and Discussion

At the starting stage, the flow field was affected mainly by the acceleration, a, and the diameter of the disk, D. A characteristic time, t_* ($t_* = \sqrt{D/a}$), can be obtained by dimensional analysis. The test results can be summarized into a curve by using the dimensionless time, $\bar{t} = t/t_*$, and the dimensionless lengths, $\bar{x} = x/D$ and $\bar{D}_v = D_v/D$.

Figure 3 shows the photographs of a typical flow in the wake of a circular disk within the starting period visualized by hydrogen bubbles. Figure 4 illustrates the flow in the wake at the starting stage. There was a circular vortex after the disk, which was the starting vortex. The center of the vortex was a circular ring having the diameter D_v. The cross-section of the

vortex ring and the xy surface gave two symmetric helical
vortexes having d_v as the approximate diameter and x_v as the
distance between the center of the vortex and the circular disk.
There was a stagnation point, S, on the ox axis. The upstream
region before point S was the backflow region and the downstream
was the forward flow region. The starting wake of the cylinder
is similar to that of a circular disk. However, there is no
separation region at the moment of starting in the wake of a
cylinder. The separation begins and the starting vortex is
formed after the boundary layer increases to a certain
thickness[1]. Since the edge of the circular disk was a sharp
closed angle, the flow separated at the edge and rolled up into a
helical vortex ring during the starting stage. However, in the
beginning of starting, the separation region and the diameter of
the vortex are very small. The starting process could be divided
into the starting stage and the transition stage. The vortex
increased in size during the starting stage and had a symmetric
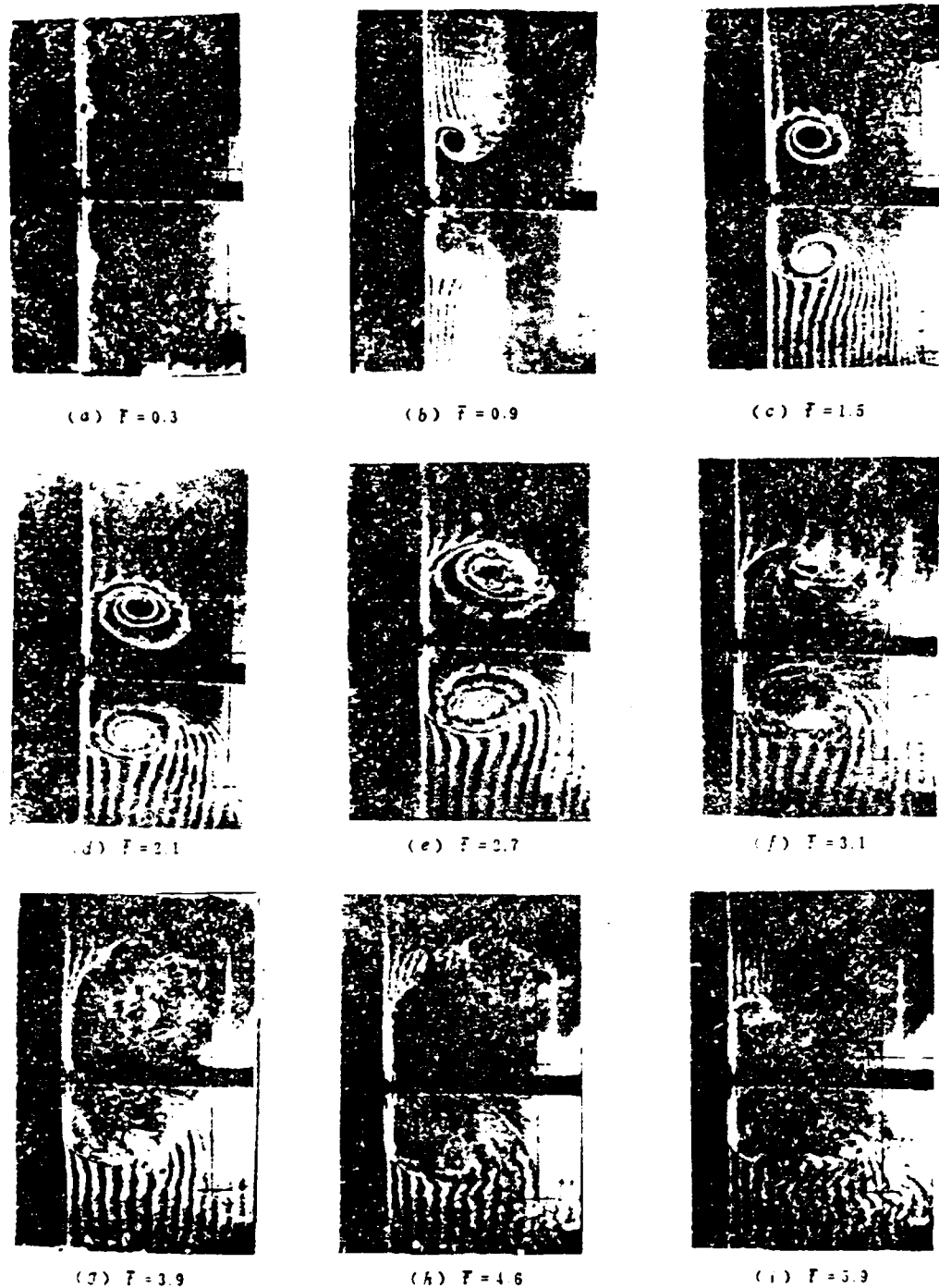configuration as shown in Figure 3(a) to 3(e). The starting

(a) $\bar{t} = 0.3$

(b) $\bar{t} = 0.9$

(c) $\bar{t} = 1.5$

(d) $\bar{t} = 2.1$

(e) $\bar{t} = 2.7$

(f) $\bar{t} = 3.1$

(g) $\bar{t} = 3.9$

(h) $\bar{t} = 4.6$

(i) $\bar{t} = 5.9$

Figure 3.   The flow visualized by hydrogen bubble method in the wake of a circular disk (D=8cm) during starting stage (acceleration a=7.43cm/s^2)

vortex became asymmetric, loose and broken during the transition /387

stage and the wake became disordered as shown in Figures 3(f) to

3(i). Both the diameter d_v and the abscissa x_v of the vortex

increased linearly during the starting stage was shown in Figure

5 and Figure 6 with $d\bar{x}_v/d\bar{t}\approx0.18$ and $d\bar{d}_v/d\bar{t}\approx0.19$. The test data

under different conditions were all falling in the same straight

line, which indicated that t_* and D were the main parameters in

the starting stage. During this starting stage, the change of

the diameter of the vortex ring, D_v was small. D_v was slightly

smaller than D during the initial period and was larger than D

during the later period. Since the diameter of the wake was

about D_v + d_v, the diameter increased linearly during the
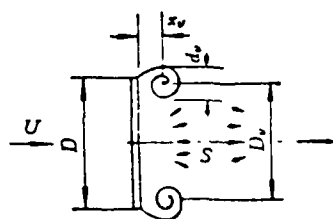
starting stage.

Figure 4. The flow in the wake of a circular disk during
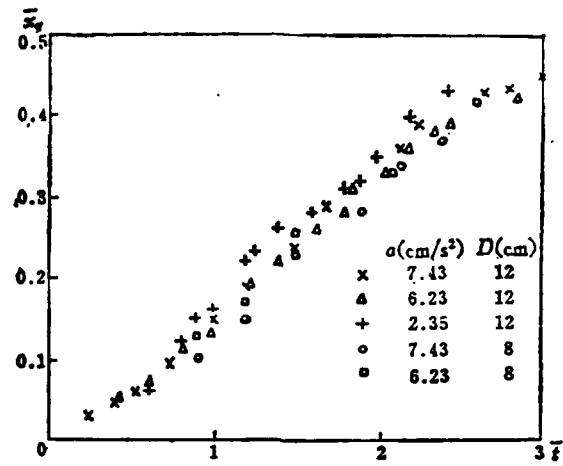   starting stage

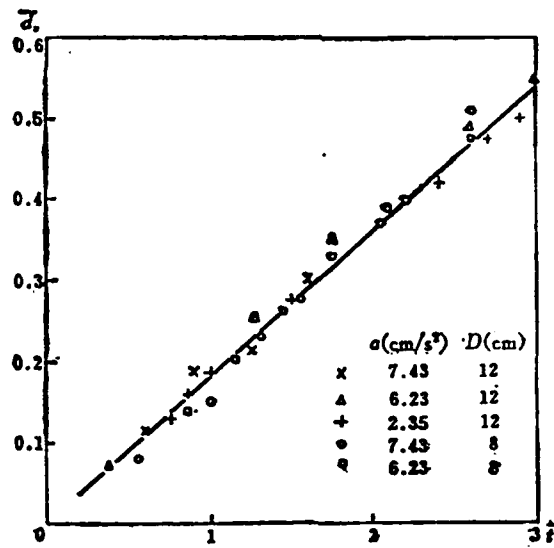Figure 5.   The abscissa of the center of the starting vortex x_v

Figure 6.   The diameter of starting vortex d_v

73

The stagnation point was on the surface of the circular disk when the starting vortex was still small. While the starting vortex grew to a certain size, the position of the stagnation point moved toward downstream and a back flow region appeared at the center of the wake. Figure 7 shows that the abscissa of the stagnation point, x_s, increases linearly with time. $d\bar{x}_s/d\bar{t} \approx 0.36$, which was approximately the sum of $d\bar{x}_v/d\bar{t}$ and $d\bar{d}_v/d\bar{t}$ since the back flow region was pushed downstream when the vorticity increased and the position of the vortex moved downstream.
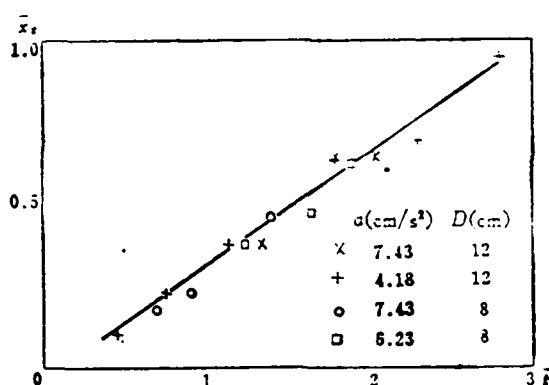

Figure 7. The abscissa of the stagnation point in the wake, x_s

During the starting stage, the vortex sheet separated from the disk edge rolled up continuously into the starting vortex. The induced back velocity increased with increasing the intensity of the vortex. Figure 8 shows the flow profile in the wake visualized by the hydrogen bubbles. The back flow speed in the wake can be determined from a series of these photographs. The results are shown in Figure 9.
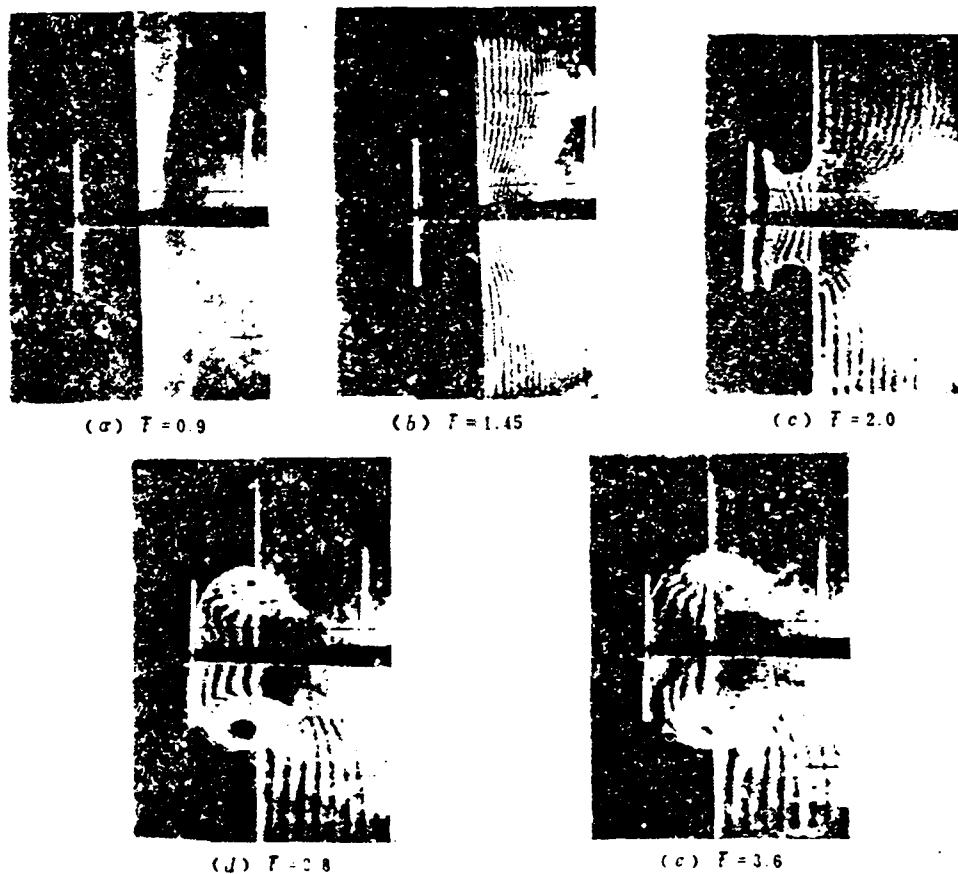
74

(a) $T = 0.9$ (b) $T = 1.45$ (c) $T = 2.0$

(d) $T = 2.8$ (c) $T = 3.6$

Figure 8. The flow in the wake of a circular disk D=8cm, a=7.43 cm/s^2, the platinum wire is located at $\bar{x} = 0.455$

The back flow peaked at the point the starting vortex was passing through the cross-section. It attained the extreme while the intensity of the starting vortex reached its maximum at the end of the starting stage. The maximum peak of the back flow occurred at about $\bar{x} = 0.65$ and $\bar{t} \approx 3.5$. The extreme value of the peak was about 1.3 times of the free stream speed which far exceeded the maximum back flow speed of the wake in steady flow (u/U is about 0.5). After the maximum back flow was reached, the starting vortex distorted and broke up and the back flow decreased gradually as shown in Figure 3(g) to 3(i).

The vortex sheet was smooth at the initial stage of the starting period as shown in Figure 3(b). Wrinkles appeared after then as shown in Figure 3(d) and the vortex sheet rolled up into small isolated vortices as shown in Figure 3(e) and Figure 10. These small vortices were continuously rolled into the starting vortex and increased the intensity of the starting vortex. Similar phenomenon was also observed in Pullin's experiment of starting vortex on two dimensional closed angle[6]. In the transition stage the small vortices no longer rolled into the starting vortex. At steady state, small vortices were observed flowing downstream along the boundary of the wake as shown in Figure 11(c). The isolated small vortices were distributed around the wake. They had irregular shape and recombined with each other continuously.
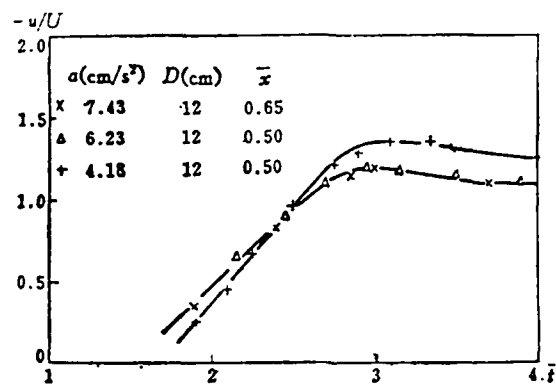
76

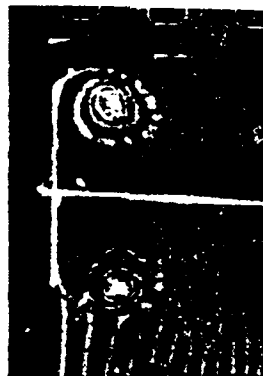Figure 9. The measured back flow speed u in the center of the
wake

Figure 10. The vortex sheet of starting vortex rolled up into

small vortices, D=12cm, a=4.12 cm/s^2

During the transition stage, the flow in the wake appeared very chaotic and violent and the wake was able to swing rather far from its centerline as shown in Figure 12 and Figure 3(i).

Figure 11. The wake of a circular disk in steady flow, D=8cm

At steady state, the flow inside the wake was turbulent containing forward and back flows as shown in 11(b). However, the flow at the boundary of the wake and the small vortices around the wake were more stable than at the transition edge. The profile of the wake approached to symmetric as shown in Figure 11(a).

/390

Figure 12. The wake in the transition stage

IV. Conclusions

1. The hydrogen bubble method for visualization of the starting flow can be used to measure the momentary flow profile and to determine the size, position and the momentary velocity profile of the vortex.

2. The speed of back flow at the center of the wake was very large during the starting stage. The maximum speed could be 1.3 times the free velocity, which far exceeds the maximum back flow speed of the wake in steady stream. The high speed of back flow might have significant influence on the drag and virtual mass of the disk. The maximum back flow speed occurred in the starting stage when the starting vortex had the maximum intensity and was about to break up. The maximum back flow speed appeared at about $\bar{x}=0.6$ while the center of the starting vortex approached the same point.

3. In the transition stage at the end of the starting period, the starting vortex became unsymmetric and broke up. In the meantime the wake was able to swing rather far from its centerline as shown in Figure 12. It might have significant effect on the material stress.

Figure 13. Model of projectile shape body, D=8cm, L=22cm; starting acceleration a=6.23m/s^2.

4. The bottoms of other bodies having sharp angle, such as warhead-like objects and parachutes, are similar to a circular disk. The flow information at the starting period is not available. Our preliminary study has shown that the flow on these objects is quite similar to that on a circular disk. Figure 13 shows the starting vortex on a hemispheric warhead-like body. The effect of the swing motion of the wake during the starting stage and the transition stage on the stress condition

on such bodies should be studied.

The author is grateful to Huang Zhen, Zhou Min-Xuan and Chang Xing for their assistance in carrying out the experiments.

References

[1] Chang, P.K., Separation of Flow, Pergmen Press, (1970).

[2] McCroskey, W.J., The Challenge of Unsteady Separating Flows, Amer. Soc. of Civil Engineering Mech. Divisions Journal Vol. 107, P. 547-563, (1981).

[3] Yun Tian-tuo et al., "The flow field of starting flow on cylindrical body", Journal of Japan Mechanic Society, Vol 5 (397), p 1298, September, 1984.

[4] Sarpkaya, T., Separated Flow about Lifting Bodies and Impulsive Flow about Cylinders, AIAA J., Vol. 4, No. 3, p. 414, (1966).

[5] Golovikin, et al, Optical Visualization of Accelerated and Decelerated Flow over a Circular Cylinder, Fluid Dynamics, Vol. 16, p. 266-271, (1981) (Translated from Izvestiya Akdemii Nauk SSSR Zhidkosti i Gaza).

[6] Pullin, D.I. and Perry, A.E., Some Flow Visualization Experiments on the Starting Vortex, J. Fluid Mech. Vol. 97, Part 2, p. 239-255, (1980).

[7] Lian Qixiang, "Tracing Methods of Flow Visualization Technology" Symposium on Flow Visualization Technology, Xiamen, 1982.

[8] Schroub, F.A. et al., Use of Hydrogen Bubbles for Quantitative Determination of Time-Dependent Velocity Fields in

Low-Speed Water Flows, J. of Basic Eng., Trans. ASME, series D, Vol. 87, No. 2, p. 429-444 (1965).

[9]   Taneda, S., et al., "Flow Visualization" (ed. Asanuma, T.) p. 209 Hemisphere, Washington, (1979).

Measurement of Turbulent Separated Flows With a

Two-dimensional LDV System

Shen Xiong and Yu Hesheng

(Tsinghua University)

Abstract

A polarized separated type of two-dimensional Laser-Doppler
Velocimeter (LDV) System is developed with a view to solving the
problem of two-dimensional measurements of a highly turbulent
separated flow having recirculating flow areas. The mean
velocity vector distribution in the turbulent separated area of
an asymmetrical step-transitioned diverging duct was measured.
Parameters relating to the location of the recirculating vortex
center and the length of the recirculating flow area were
obtained. Furthermore, some of the experimental results were
compared with the numerical analog results.

Introduction

The turbulent separated flow in an asymmetrical step-
transitioned diverging duct has been noted to have some
significance in many engineering problems. Being characterized
by simplicity in structure and ease of construction as well as
relatively fixed positioning of the separation point and the
separation area in space, it is handy to do experimental work and
theoretical research on it. Although many scientists and

scholars have been conducting a host of experiments on the highly

turbulent recirculating flow in ducts or in channels over recent

years, most of their results however, have been one-

dimensional[1,2]. It is seldom to see simultaneous measurements

being made of two-dimensional velocity components. Flow field

parameters of similar ducts were measured using a homemade one-

dimensional frequency-shifting laser velocimeter/system. The

problems with this set-up are that it is difficult to determine

both the velocity vector distribution in the separation area and

the precise location of the center of the recirculating flow

area[3]. Nor is it possible to give rise to more data for

numerical calculations. It is possible, however, as cited by

some references, to infer or deduce the stream line and the

recirculating center from the axial velocity profile and the

integration of the flow[4]; or to conduct multiple one-

dimensional measurements along difference directions so that flow

parameters in two-dimensional[2] flow could be obtained. But all

these will not only add tremendous amount of work to

experimentation and data processing but also affect the accuracy

of measurements as well. It is therefore the purpose of this

paper to use a homemade Laser-Doppler Velocimeter (known as LDV

in short, hereinafter) system, that is capable of simultaneously

measuring two-dimensional velocity components, to conduct

detailed measurements of the turbulent separation flow in an

asymmetrical step-transitioned diverging duct in order to obtain

the mean velocity vector distribution, axial (along x-axis) and

vertical (along the y-axis) distributions of various turbulence

intensities, Reynolds stress distribution and other important parameters such as recirculating center and the location of the re-attachment point, etc., with the objective of accumulating data for further theoretical and experimental researches.

II. Instrumentation and Experimental Set-up

1. Two-dimensional LDV Optical Path

The polarized separated type 2-D LDV System (Figure 1) developed employs a low-powered helium-argon laser as its light source. The optical part consists of the laser, the incident optical element, the separation element for scattered light and the frequency-shift element. The function of the incident light element is to convert the light-beam emitted from the laser into three beams of parallel light that intersect the plane perpendicular to the light axis at three points. These three points form an isosceles right triangle as shown in the left lower part of Figure 1. Light beam I is normal to beam II at 90° with each other in the direction of polarization,

---

beam I thus forms an angle of polarization of 45° with both beam   /394 II and beam III. These three light beams are focused through the focusing lens onto the measuring point forming two sets of mutually perpendicular interference light fringes within the object being measured (Figure 2). The frequency shifting device

consists of an acoustic optical modulator and a driving unit for frequency shifting. A first degree diffracted light with frequency equal to the frequency of the driving source could be obtained by inserting an acoustic optical modulator into the incoming light beam. [5] Thus, if all three light beams are each inserted with an acoustic optical modulator and the three first order diffracted beams are focused into one, two sets of shifting interference light fringes could be obtained within the object being measured through the allocation of different frequencies. This is what is called the differential mode of three devices of the two-dimensional LDV. A driving frequency of around 40 MegaHertz for the acoustic optical modulator was chosen. Different amounts of frequency shift could be selected, ranging from
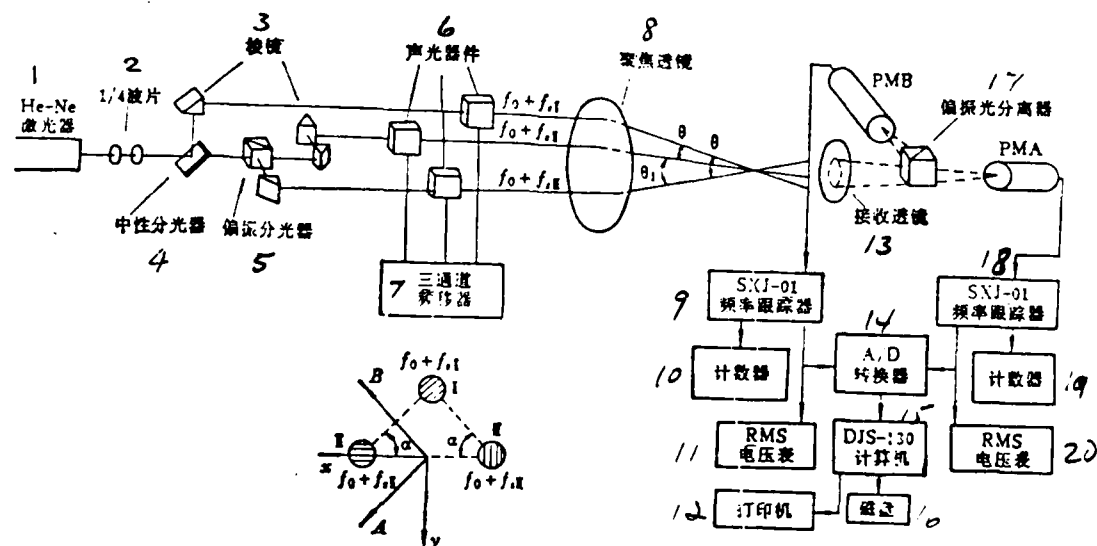

Figure 1. Schematic Diagram of the 2-D LDV System

1. He-Ne laser
2. 1/4 waveguide
3. prisms
4. neutral beam splitter
5. polarized spectroscope
6. opto-acoustic device
7. 3-channel frequency shifter
8. focusing lens
9. frequency tracker, Model SXJ-01
10. counter
11. RMS voltmeter
12. printer
13. receiving lens
14. A/D converter
15. DJS-130 computer
16. magnetic-disk
17. polarized spectroscope
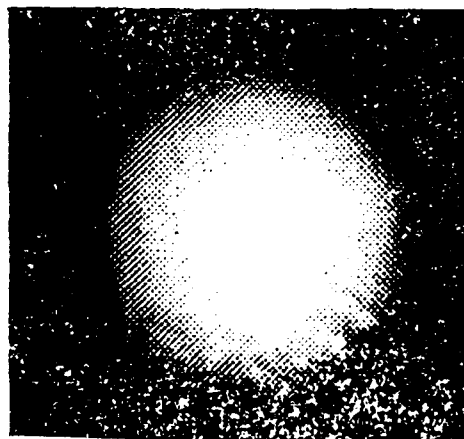18. SXJ-01 frequency tracker
19. counter
20. RMS voltmeter

Figure 2. Orthogonal Interference Fringe Pattern in Control Volume

4.5 Kilohertz to 7.5 MegaHertz with a total of 14 bands of
frequency shift by using a three-channel frequency-shift driver.
The advantage of the differential mode is that the required
frequency shift could be obtained directly from the optical mixer
without the use of an electronic mixer. Since the frequency
shift thus obtained is normally much smaller than that of the
driving frequency, it is therefore possible to use a photoelectric
device with low frequency response. The two velocity components
in the scattered light receiver are separated by means of a
polarized spectroscope. The horizontally polarized light
transmission and the reflection of the vertically polarized light
will separately shine onto the photoelectric multiplier based on
the principle of the light separation by polarization. Since   /395
only one receiving lens is sufficient to effect two-dimensional
measurement with monochromatic light, the scheme discussed in
this paper is simple in construction and easy to use.
Theoretically speaking, however, plane light waves with certain
polarized characteristics once scattered will change their
polarization characteristics. It is because of this phenomenon
that although the planes of polarization of the incident light
are perpendicular to each other, the planes of polarization of
scattered waves may not necessarily remain perpendicular to each
other after scattering. This is the so-called "cross-interference"
or "deviation effect". This effect can also be observed during
the experimental process. But, under conditions of using forward
scattering and when the scattered particles are relatively tiny
in size, the cross-interference between the two channels will

generally not exceed 10%, which will ensure proper functioning of the frequency tracker used in the experiment.

2. Flow Test Model

The flow test model used is made from plexiglass. Figure 3 shows its inside dimensions. The flow medium used is running water which contains sufficient amounts of natural particles. The circulating water system consists of water pump, water tank, flowmeter and duct valve system, etc.
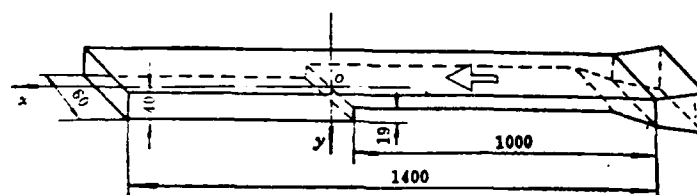

Figure 3.   Inside Dimensions of the Test Model

Experiments were conducted and completed at Reynolds numbers $Re_H = 5900$ and 8340 with length scale equal to the step height. The corresponding mean axial velocities at the inlet cross-section are 0.317m/s and 0.444m/s, respectively.

The test plane lies in the plane of symmetry of the duct. For measurements to cover the entire turbulent separated region and for a more detailed distribution of data points, a total of 30 cross-sections ranging from $x/H = -0.5$ to 7.25 were measured. Closer measurements were made in the recirculating flow area

transversely at an interval of every 2mm, resulting in a total of 450 measuring points.

The test model is mounted on a mobile coordinate frame having 4 degrees of freedom (Figure 4), so that location of measuring points could be varied. The positioning accuracy of /396 the coordinates is 0.01mm.
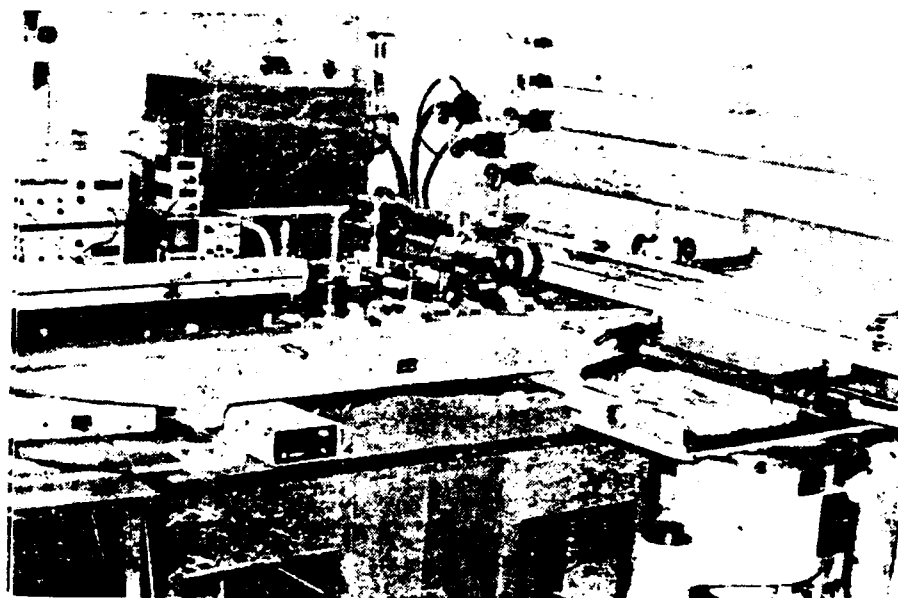

Figure 4. Photograph of the Experimental Set-up

3. Signals and Data Processing

The Doppler signals from the two channels generated by the photoelectric converter are processed separately by two frequency trackers. The frequency outputs from the two frequency trackers are averaged in numerical counts separately by using two digital

90

frequency meters in order to achieve higher measuring accuracy of the mean velocities. Sampling time is 10 seconds. The average values obtained from ten samplings are again averaged. This operation will give an integrated mean time corresponding to 100 seconds. Moreover, it accurately measures the actual values of the medium frequencies of the frequency tracker over the entire measuring range, whereby the Doppler frequency measured can be calculated. With all these provisions, the accuracy of measurement of the mean velocity could be better than 0.2%, which will be equivalent to a velocity resolution of around 0.4mm/s. It is thus possible to relatively accurately measure and locate the positions of both the center of the recirculating flow region and the re-attachment point.

The level of turbulence and the Reynolds stress are obtained from the analog output of the frequency tracker as indicated by the RMS voltmeter and subsequent calculations[6]. It can also be achieved directly through a proper software by using microprocessor processing the analog signals of the instantaneous velocity converted by A/D converter to obtain such statistical characteristics as the mean velocity, level of turbulence, Reynolds stress, the density function of velocity probability and power spectrum, etc.

III. Results of Experiments and Discussion

The mean velocity vector, the axial and vertical components of the mean velocity, the level of turbulence and distribution of

91

Reynolds stress are shown in Figure 5 through Figure 8 at the condition of $Re_H=5900$. Except that the Reynolds stress is non-dimensionalized by adopting the U^2_{max}, the rest are all non-dimensionalized by using U_{max}, which is the hourly mean value at the cross-section of $x/H=-0.5$ when the velocity is maximum along the x direction.

1. Distribution of the Mean Velocity (Figure 5 and 6)

The vertical mean velocity is smaller than the axial mean velocity by almost two orders of magnitude in most of the main flow region. The average flow lines are nearly parallel. The axial velocity drastically decreases while the vertical velocity increases within the shear layer, resulting in a gradual transition to the recirculating flow region. At $Re_H=5900$ and

8340, the recirculating center lies at x/H=3.2, y/H=0.42 and x/H=3.1, y/H=0.41 respectively. The re-attachment points lie at x/H=7 and x/H=7.4 respectively. The maximum reverse mean velocity is around 0.24 U_{max} at locations below the re-circulating flow center.
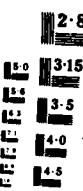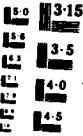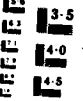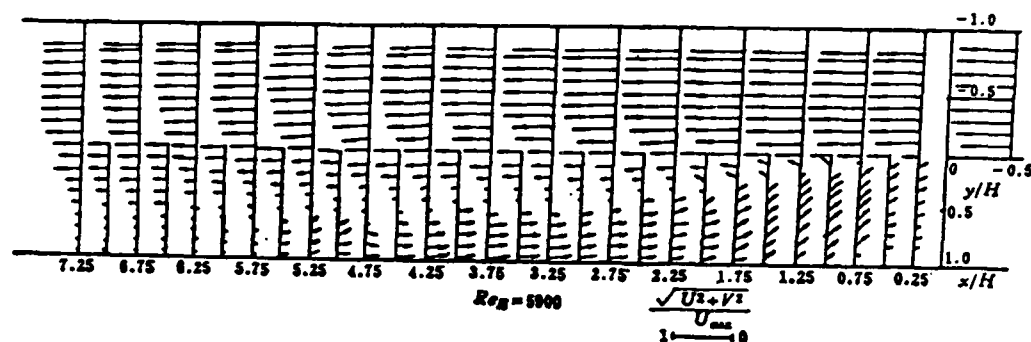
Figure 5. Measured Mean Velocity Vector Distributions in the 2-D Duct

For comparison with the results of numerical calculations given in reference [7], two-dimensional measurements were also made at the cross-section shown in Figure 9 at condition Re_H=5588. The axial mean velocity (Figure 9(a)) is non-dimensionalized with the mean axial velocity hourly mean value U_m at cross-section of x/H=0.25. Numerical values are calculated by using the two-equation K-ε turbulent model; except for the span height ratio which is 4, all other geometrical parameters are identical. The lengths of the recirculating flow region given in Reference [3 and 7] are 6.880 and 6.86 respectively while the length given in this paper under condition of relevant Re_H is 6.95. The three figures are basically in good agreement.
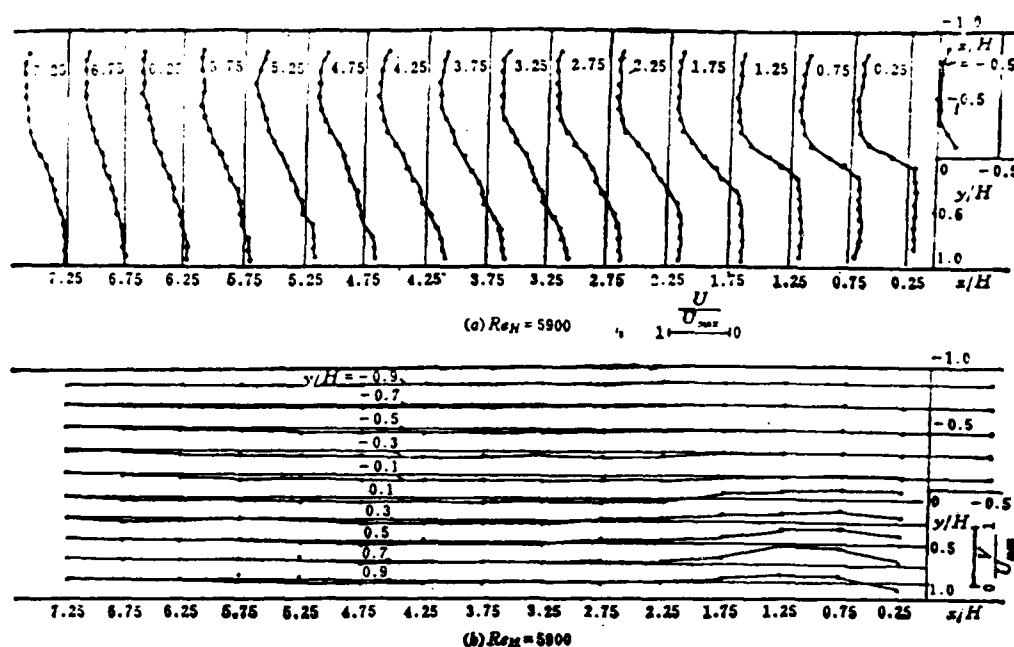
Figure 6. Measured (a) axial and (b) vertical mean velocity
distributions in the 2-D duct

2. Distribution of the Levels of Turbulence

Figure 7 shows the axial and the vertical distributions of
the levels of turbulence. It may be noted that differences exist
in both the pattern of distribution and in quantity. In areas
near the upper wall surface, axial fluctuations increase while
the vertical pulsations tend to diminish. This phenomenon is not
apparent in locations near the lower wall surface.

In the turbulent shearing layer downstream of the step,
pulsations significantly increase. The maximum pulsation is
nearly more than threefold the pulsation location of the inlet
center. These findings basically agree with those given in
references [2 and 3].

94

Various statistical mean times were chosen to determine the duration of mean time that should be used during a measuring operation. As the mean time reaches 50 sec, the discrete distribution of the mean time is less than ±0.2%, which may be regarded that process has been stabilized and the estimated maximum period of pulsations around 1 sec. to several seconds. It is believed that the statistical mean time needed for the inlet cross-section center area is much less. Therefore, it is obvious that the part having large scale pulsation in the separated flow area is considerably increased than that at the inlet flow region. Data processing must therefore be conducted over a sufficiently long statistical mean time in order to ensure proper accuracy in measuring the mean velocity.

The turbulent kinetic energy calculated by the 2-D measured value method discussed in this paper basically agrees with the result from numerical value calculation [Figure 9(b)]. Since it is impossible to measure the 3-D pulsating velocity, the experimental turbulent kinetic energy is obtained in approximation by the equation $K = \frac{1}{2}(u'^2 + 2v'^2)$
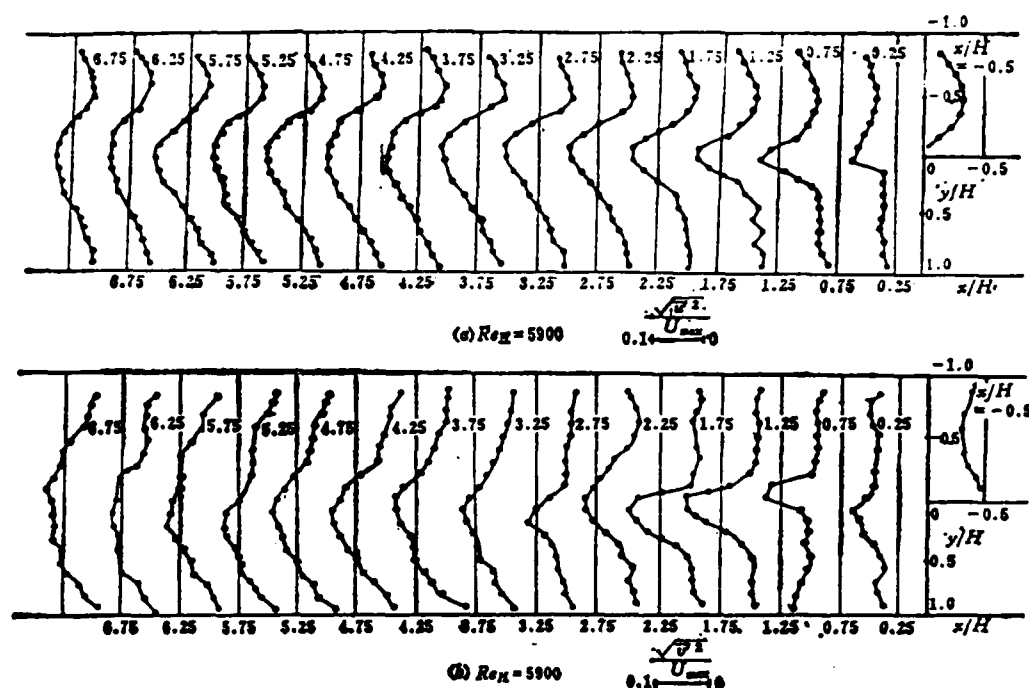
Figure 7.   Measured (a) Axial and (b) Vertical Turbulence
Intensity Distribution in the 2-D Duct

3.   Distribution of Reynolds Stress

Figure 8 shows the non-dimensionlized Reynolds stress
distribution obtained through data operations.   At locations near
the upper wall surface, the Reynolds stress changes its sign and
becomes negative.   The Reynolds stress significantly increases in
the shear layer and attains its maximum value.   At locations
close to the lower surface, however, the Reynolds stress appears
smaller because of a smaller gradient of the mean velocity within
the recirculating flow region.   These trends agree with those
results given in reference [2].   But there are noticeable
differences in the maximum values of the Reynolds stress and
their locations.   The maximum value of Reynolds stress reported

96

in this paper is around 0.011 (in terms of non-dimensionalized U^2_{max}), which is smaller than that shown in reference [2]. On the other hand, the discreteness of data obtained in this paper is considerably less.
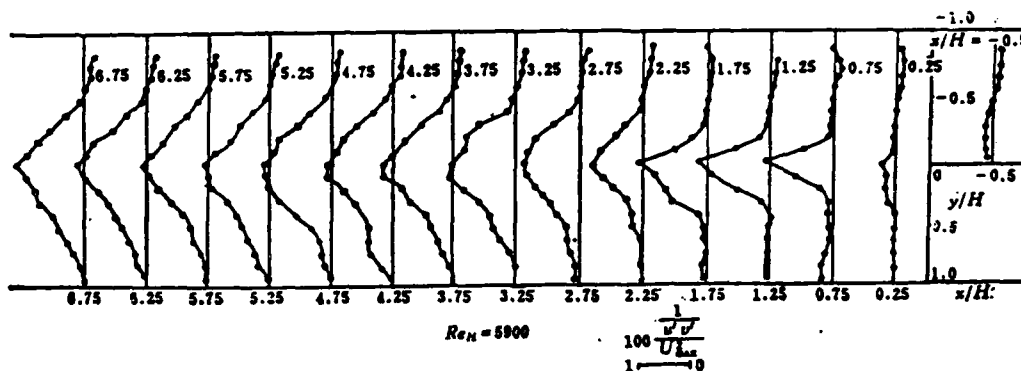

Figure 8.   Measured Reynolds Stress Distributions in the 2-D Duct

The differences in numerical values are due to the greater errors in data processing. Moreover, the method of measurement as well as the flow medium employed in this paper are also different from those cited in reference [2]. Because of the fact that experimental results in this respect have been lacking, only /399 rough comparisons are possible. It is therefore worthwhile to go into more detailed research in this respect both experimentally and analytically.
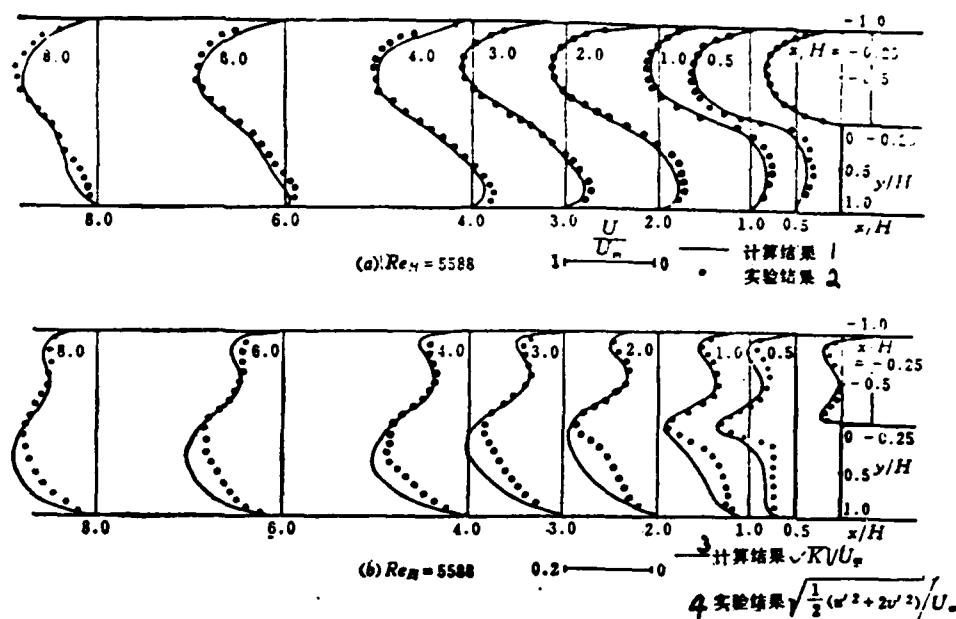
Figure 9. Comparisons of Experimental and Computed Values of
(a) Axial Mean Velocity and (b) Turbulent Kinetic
Energy in the 2-D Duct

1. computed results
2. experimental results
3. computed results
4. experimental results

IV. Conclusions

The turbulent separated flow could be more accurately
measured with a two-dimensional Laser-Doppler Voltmeter (LDV)
system having frequency-shift device. Important parameters, such
as the two-dimensional mean velocities in the turbulent shear
layer and the recirculating flow region, the pulsating velocity
and the Reynolds stress distribution as well as the location of
the recirculating flow center, and the length of the
recirculating flow area, could be obtained.

Experimental results indicate the turbulent separated flow generated in a stepped diverging duct has part of its areas where axial velocity and vertical velocity are widely different. While in others, such as the recirculating flow region, where the mean velocity may tend to become zero and the turbulent intensity as well as the time scale of pulsation are quite strong, consequently, it is impossible to ensure a certain desired accuracy in 2-D measurement (chiefly in the vertical direction) if the measuring system is not both equipped with sufficiently high velocity resolution and uses sufficiently long mean time.

In order to further and better understand the mechanism of the flow in a stepped diverging duct and acquire the various flow parameters of a 3-D flow region, it is significant to explore and research into the three-dimensional laser velocimeter system.

References

[1] Durst, F. and Tropea, C., Turbulent Backward-Facing Step Flows in Two-Dimensional Ducts and Channels, Proceedings of the Third Symposium on Turbulent Shear Flows, 18,(1981).

[2] Stevenson, W.H., Thompson, H.D. and Craig, R.C., Laser Velocimeter Measurement in Highly Turbulent Recirculating Flows, Engineering Applications of Laser Velocimetry, 163, (1982).

[3] Shen Xiong, Liao Husheng, Measurement High Level Turbulent Recirculating Flows with Frequency Shift Laser Velocimeter System, Academic Report on Mechanics, 5, (1982).

[4] Freeman, A.R., Laser Anemometer Measurements in the
     Recirculating Region Downstream of a Sudden Pipe Expansion,   /400
     Proc. of the LDA-Symposium, Copenhagen, (1975).

[5] Shen Xiong, Liao Husheng, Laser Velocimeter System with
     Optical Frequency Shift, ((Laser)) Journal, 10, (1982).

[6] Durst, F. and Whitelaw, J.H., Measurements of Mean Velocity,
     Fluctuating Velocity, and Shear Stress in Air Using a
     Single Channel Optical Anemometer, DISA Information, No 12,
     (1971).

[7] Hong Juntao, Numerical Analog of Turbulent Separated Flows
     in a Two-Dimensional Asymmetrical Sudden Expanding Channel,
     Thesis for M.S. Degree of Qinghua University, (1983).

[8] Abbott, D.E. and Kline, K.J., Experimental Investigation of
     Subsonic Turbulent Flow Over Single and Double Backward
     Facing Steps, J. Basic Engng., Trans. of ASME, Sept.(1962).

[9] Denham, M.K., A Directionally-Sensitive Laser Anemometer
     for Velocity Measurements in Highly Turbulent Flows, J.
     Physics E, Scientific Instruments, 8, (1975).

An Experimental Investigation of the Location of the Boundary

Layer Transition Area on the Airfoil NACA0012 Using Surface

Hot Film Gauges

Wang Tiecheng

(Nanjing Aeronautical Institute)

Abstract

Experimental research on the location of boundary layer transition area on the airfoil NACA0012 using M-1 type surface hot film gauges developed by the author and colleagues is discussed in this paper. The location of the boundary layer transition area varies as the angle of attack of the airfoil changes as shown in Figure 3. Experimental results showed that the application of this technique yielded satisfactory results.

I. Introduction

The measurement of the location of the transition area from laminar flow to the turbulent flow on the boundary layer on a solid wall surface is quite an important task of measurement. There are quite a few methods of making this measurement, one of which is the use of surface hot film gauges. The features of this method include: less disturbance to the flow as compared to the probe method, ease of making measurements and less sensitive to noise and pressure gradient variations, etc.

Application of the surface hot film gauges for measuring the

boundary layer transition has been mentioned in some published papers [see references 1 and 2]. The features of the experiment discussed in this paper in comparison with those cited in the above mentioned references are that many surface hot film gauges are glued to the upper surface of the airfoil for locating the transition area, and the hot film signals are displayed by using three different kinds of displaying instruments for the purpose of cross checking and comparison to determine the location of the transition area at different angles of attack.

II. Principles of Operation

The principle of operation of the probe method and the laser velocimetry for the measurement of the boundary layer transition are all based on the fact that there are apparent differences in velocity modes and levels of turbulence of the laminar flow boundary and the turbulent flow boundary layer. Unlike the principles of operation of the two methods given above, the surface hot film gauge method is based on the difference in the variations in the shear stresses on the wall surface of the laminar flow boundary and the turbulent flow boundary for the measurement of the boundary layer transition. This means that under the same Reynolds number, the shear stress on the wall surface of the laminar flow region (corresponding to hourly mean value of the turbulent flow) is much less than that of the turbulent flow region. Also, its root-mean-square value is smaller in the laminar flow region and larger in the turbulent

102

flow region. Moreover, the pulsating wave forms are strikingly different in these two different flow regions. The hot films glued to the surface of the model when connected with the CTA circuit (i.e., the constant temperature type hot-wire hot-film anemometer) could be used with different displaying instruments for the measurement of the above three quantities (i.e., the relative variations) to determine the location of the transition area. Reference [3] shows the concrete way of making the measurement.

Since it is only necessary to measure and determine the relative variations in shear stresses on the wall surface, use of the technique described in references [1,2] could be made in the experiment on the measurement and determination of the boundary layer transition. The technique includes using directly the output voltage E from the CTA circuit (the RMS value) to represent the wall surface shear stress (the hourly mean value); the pulsating voltage E_{rms} (also the RMS values) to indicate the root-mean-square value of the shear stress on the pulsating wall surface; the oscillogram of voltage shows the pulse wave form of the shear stress of the wall surface. Both the values of E and E_{rms} are obtained by subtracting their respective initial readings.

III. The Experiment

Experiments were conducted in 1983 at the Nanjing Aeronautical Institute with a 2-D low-level-turbulence wind

tunnel. The experimental section of the wind tunnel has a length of 6m, width 0.3m, height 1.2m. The maximum wind speed attainable is 42m/s, level of turbulence is less than 0.08%. The chord length of the NACA0012 Airfoil Model is b=0.15m, and the span length is 0.3m. The model was placed in the experimental section straddling across the two side walls. Beginning from the leading edge, the distance is expressed in terms of x chordwise. One M-1 type hot film was glued at each of the stations having x/b=0.4, 0.5, 0.6, 0.7 and 0.8 to the upper surface of model airfoil. The length of the hot film (heat generating film) in the direction of the airstream is 0.05mm approximately, thickness about 0.005mm. The substrate thickness of the film is around 0.03mm. Shallow grooves were engraved where hot films were to be glued to the surface of the airfoil model prior to the gluing operation. It is required that hot films once glued, its base should fit thoroughly with the airfoil model surface without forming any ruggedness.

A tsi1050 type hot wire, hot film anemometer was used in the experiment. The three displaying instruments used consist of tsi1050 digital voltmeter (for measuring mean value of E), tsi1070 type root-mean-square-valued voltmeter (for measuring E_{rms}) and MS-5511 memory oscilloscope (showing pulse wave form).

Experimental Results

Figure 1 and Figure 2 show the experimental results. Figure 1 shows respectively the variations of E and E_{rms} with the angle

of attack α at various stations of x/b. Figure 3 shows the
oscillograms of 5 typical angles of attack for x/b=0.7. The
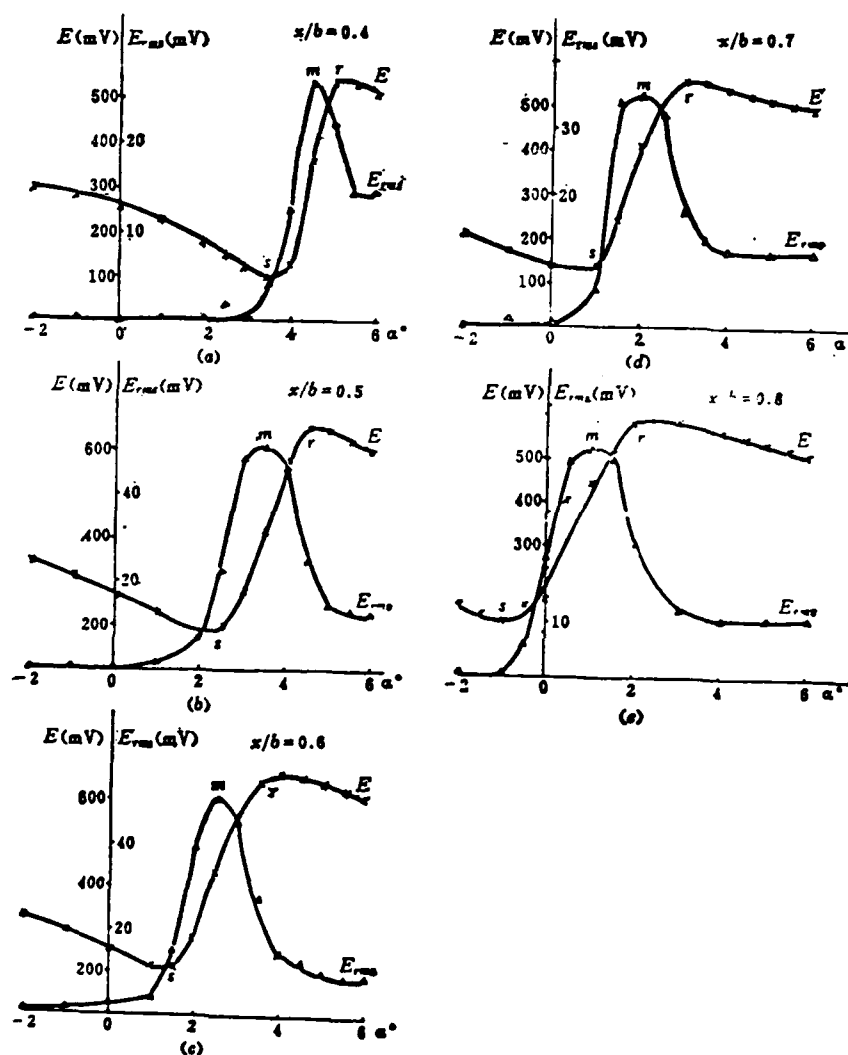vertical deflection sensitivity as well as the scanning

Figure 1. Variations of E and E_{rms} With the Angle of Attack
at Different x/b Stations

x - output voltage E
- RMS of voltage pulse E_{rms}

speed of the oscilloscope remain unchanged throughout the experiment. Each big division in the horizontal direction is 2ms. Similar wave forms could also be found at other x/b stations. The Reynolds number used in the experiment is $Re_b = \rho v_\infty$ /403 b/$\mu = 2 \times 10^5$.
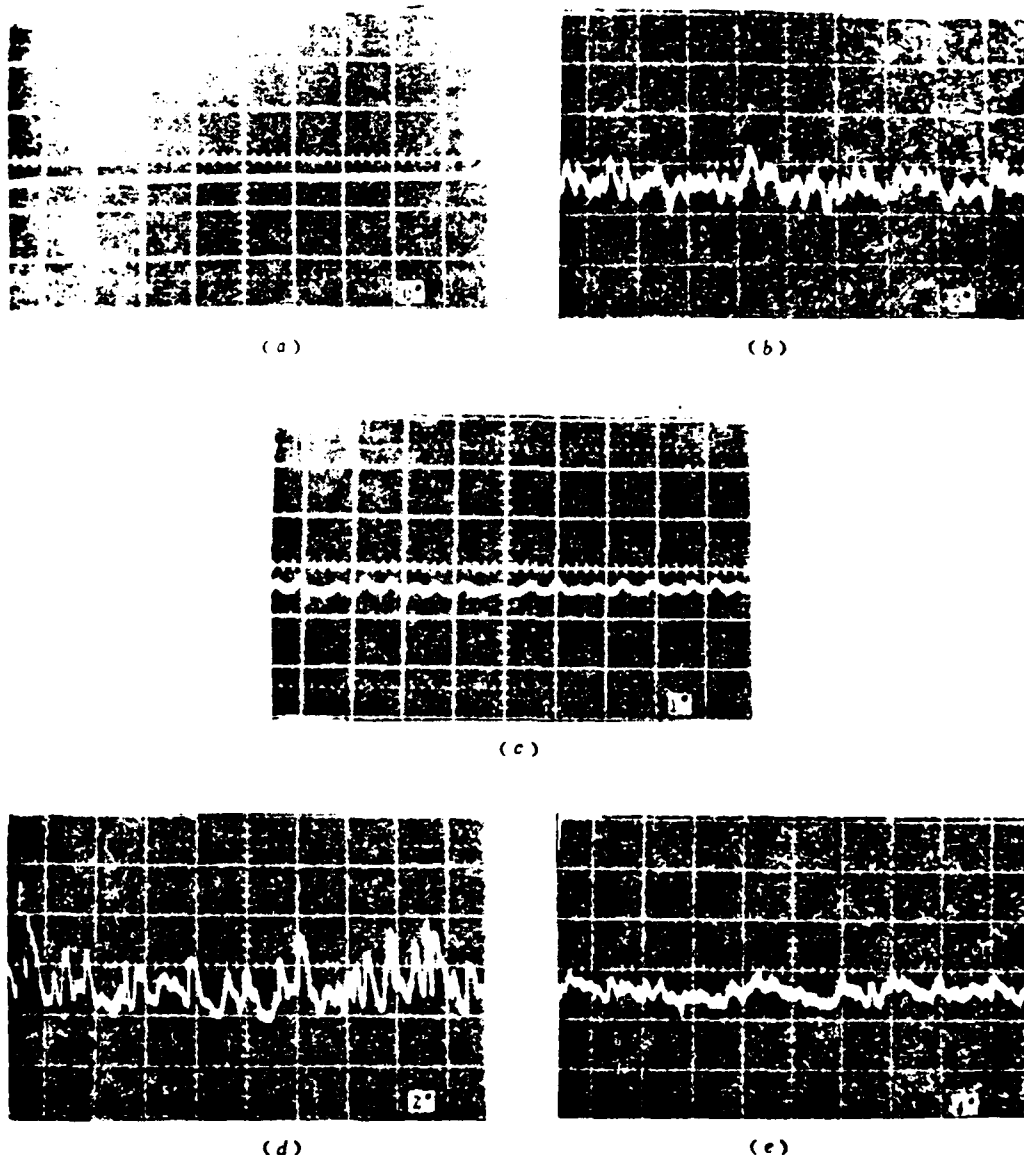

(a)

(b)

(c)

(d)

(e)

Figure 2. The Oscillograms of the Voltage From Surface Hot Film Gauge at x/b=0.7

NACA0012 is one of the typical airfoils of medium thickness; its maximum thickness is located at 30% of chord length measured from the leading edge. It can be assumed that the locations to which hot films are glued (i.e., x/b=0.4, 0.5...) are all well within the region of converse pressure gradient for the range of attack during the experimental process. The greater the angle of attack the steeper the gradient of converse pressure. It can be observed from Figure 2 that oscillograms showing the variation of E with angle of attack diminish with an increase in the angle of attack but suddenly shoot up to a certain point after which they drop again. Let s and r represent the lowest point and the highest respectively, it can be noted that apparently instability occurs within the flow starting from point s. Point r depicts that the flow has completely turned into turbulence point r is   /404 the so-called transition point. Figure 2 also shows the variation of E_{rms} (α) curve. Let m be the point; point m lies in-between s and r. The various locations of s, r and m in Figure 2 are designated by x/b and α on the coordinate paper. The three lines connecting S, R and M will respectively form three discrete curves as shown in Figure 3. The location and extent of the transition region at various angles of attack for an airfoil can be determined by using these curves. The results so obtained basically agree with the regular pattern that the transition point moves forward as the converse pressure gradient increases. The experimental points x and + in Figure 3 were taken from the Appendix of Reference [1] and an extrapolated value from Reference [4] respectively. The results also agree

107

fairly well with the experimental results discussed in this
paper.
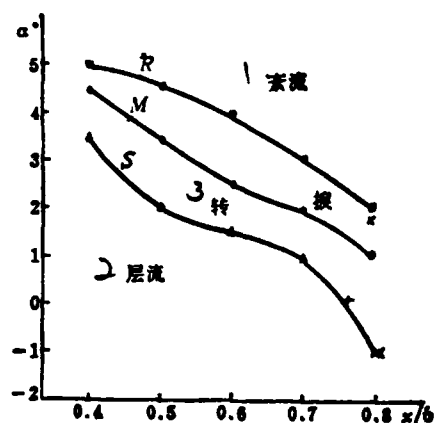

Figure 3. The Locations of Boundary Layer Transitions as
          Determined from the Experiments

          1. Turbulent Flow
          2. Laminar Flow
          3. Transition

Conclusions

1. Surface hot film is an ideal element for the measurement
and determination of boundary layer transitions.

2. The experimental technique of determining the locations
of the boundary layer transition region from using a number of
surface hot films through the measurement of the output voltage
of the CTA circuit, the root-mean-square value E_{rms} of the pulse
voltage as well as the voltage oscillograms is promising.

Acknowledgement

References

[1] McCrosky, W.J. and Durbin, E.J., Flow Angle and Shear Stress Measurements Using Heated Films and Wires, AIAA J. Vol. 8, No. 3 (1970), pp. 518-523.

[2] Meier, H.U., Kreplin, H.-P. and Fang, L.W., Experimental Study of Two- and Three-Dimensional Boundary Layer Separation, DFVLR IB222 81A12(1981).

[3] Wang Tiecheng, Principles, Construction and Application of the Surface Hot Films. Corpus of Catalogues of these read on the Annual Symposium of the Institute of Aeronautics of China, No. 8215001 (1982).

[4] Lin, C.C., Turbulent Flow and Heat Transfer, Princeton University Press (1959), P. 58.

END
DTIC
8-86